Chapter 3

Alpha Collector - Description

3.1 Introduction

TFTR has previously relied on the lost alpha scintillator detectors (Sec. 2.5.1) as the sole escaping alpha diagnostic. In order to provide a complementary measurement of escaping alphas, a new alpha collector sample probe [23, 24] has been developed. The alpha collector probe operates on an entirely different physical principle, i.e. the implantation and subsequent trapping of alpha particles in nickel foils [25]. This detection technique offers several improvements over the scintillator method. In particular, the primary reasons this detection technique was selected are:

1. for improvement of the energy resolution with respect to the lost alpha scintillators;
2. for its inherent ease of absolute calibration, allowing a valuable cross calibration for the lost alpha scintillators and validation of alpha loss models;
3. for its immunity to high neutron fluxes, which may prove useful in ITER and future DT reactors.

A general overview of the detection technique is described in Sec. 3.2. The specifics of the probe head design and many of the factors that drove design choices are presented in Sec. 3.3. The sample analysis method used to measure helium content in individual nickel foils is covered in Sec. 3.4. The geometry of the alpha collector with respect to components and α–particle orbits within TFTR is discussed in Sec. 3.5, and finally, the alpha collector is compared and contrasted to the lost alpha scintillator detectors in Sec. 3.6.

3.2 Detection Technique

The alpha collector probe [23, 24] is based on the foil deposition technique originally proposed by Langley [25]. Similar methods have been previously used on TFTR to

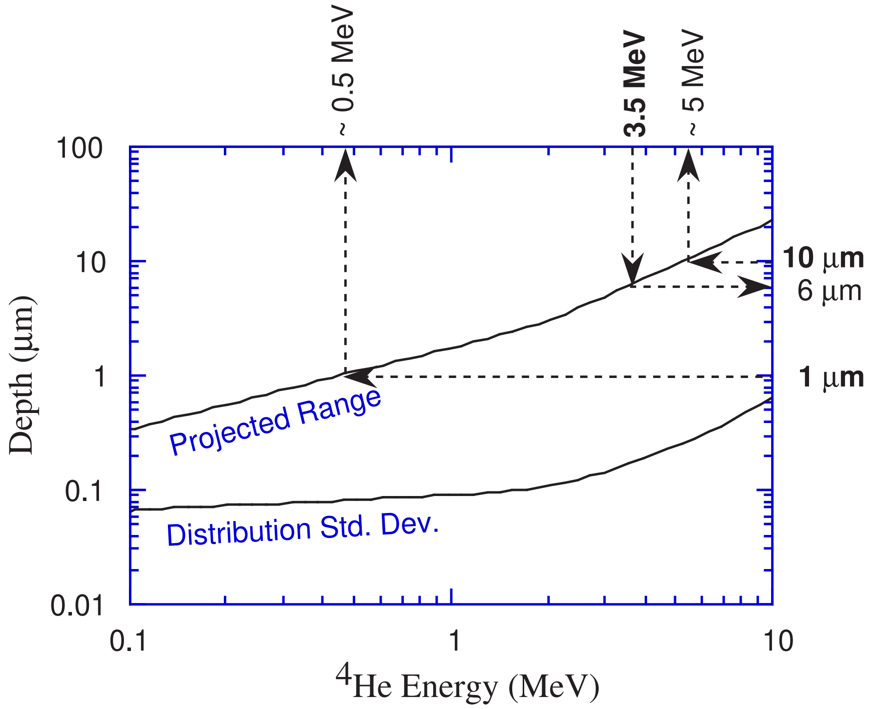

Figure 3.1: *Projected implantation range and standard deviation (straggling) for ^{4}He implanted into nickel. Birth energy alphas at 3.5 MeV travel $\sim$ 6 μm. Energy detection range for 1–10 μm of nickel is $\approx$0.5–5.0 MeV. (Taken from Ref. [29])*

collect DD fusion produced tritons [26], and on the Joint European Torus (JET) to collect ^{3}He ions accelerated by ICRH [27, 28]. In the current TFTR implementation of this technique, escaping alpha particles whose trajectories intercept the detector are implanted into a stack of nickel foils consisting of ten layers of 1 μm thick foil. This is sufficient to stop DT fusion alphas at 3.5 MeV, which have a projected penetration range of 6 μm in nickel [29] as seen in Fig. 3.1. The alpha particles form a distribution of implantation ranges in the foil stack that is dependent on their incident angles and energies. Once the alphas are stopped in the Ni, they are trapped and remain immobile as long as the Ni remains below a critical temperature of $\sim 400°$ C [30, 31].

The foils are removed from the TFTR vacuum vessel after exposure to the alpha flux of one or more discharges. They are then analyzed for He content by melting the foils one at a time in an off-site vacuum chamber (located at the University of Toronto), thus releasing the He, and then measuring the partial pressure of He with

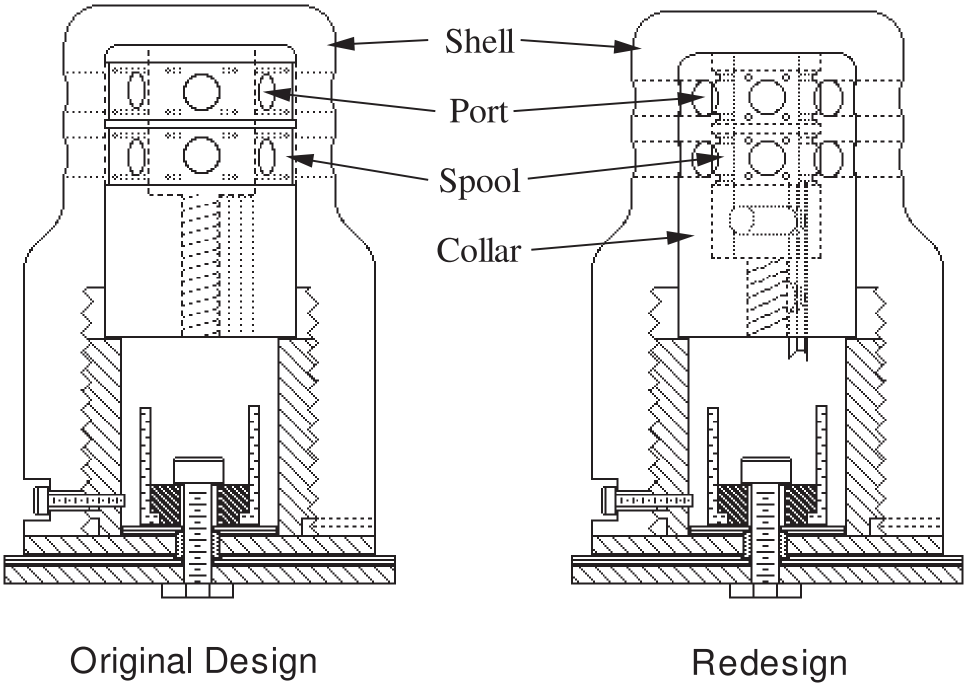

Figure 3.2: *(a) Original design and (b) redesign of alpha collector probe head. Head consists of outer shell which houses 1/4 in deep collimating ports, inner spool on which the nickel foils are wrapped, collar in the redesign shown in (b) which extends the collimating ports to 1/2 in, and supporting components to provide electrical isolation and mount to TFTR bottom probe located in bay-D.*

a Residual Gas Analyzer [23, 32]. The alpha energy spectrum is then inferred from the range distribution of He in the Ni foil stack. Calibration implants of known energies and total fluences (Sec. 3.4.2) have been used to check the accuracy of the implantation model (Sec. 4.2) and sample analysis method (Sec. 3.4.1).

3.3 Probe Head Design

The two alpha collector probe head designs used are shown in Fig. 3.2. Feature dimensions for the original design are specified in Fig. 3.3. The probe head consists of nickel foils held by a spool piece which is inserted into a shell. The shell is made of a 4D

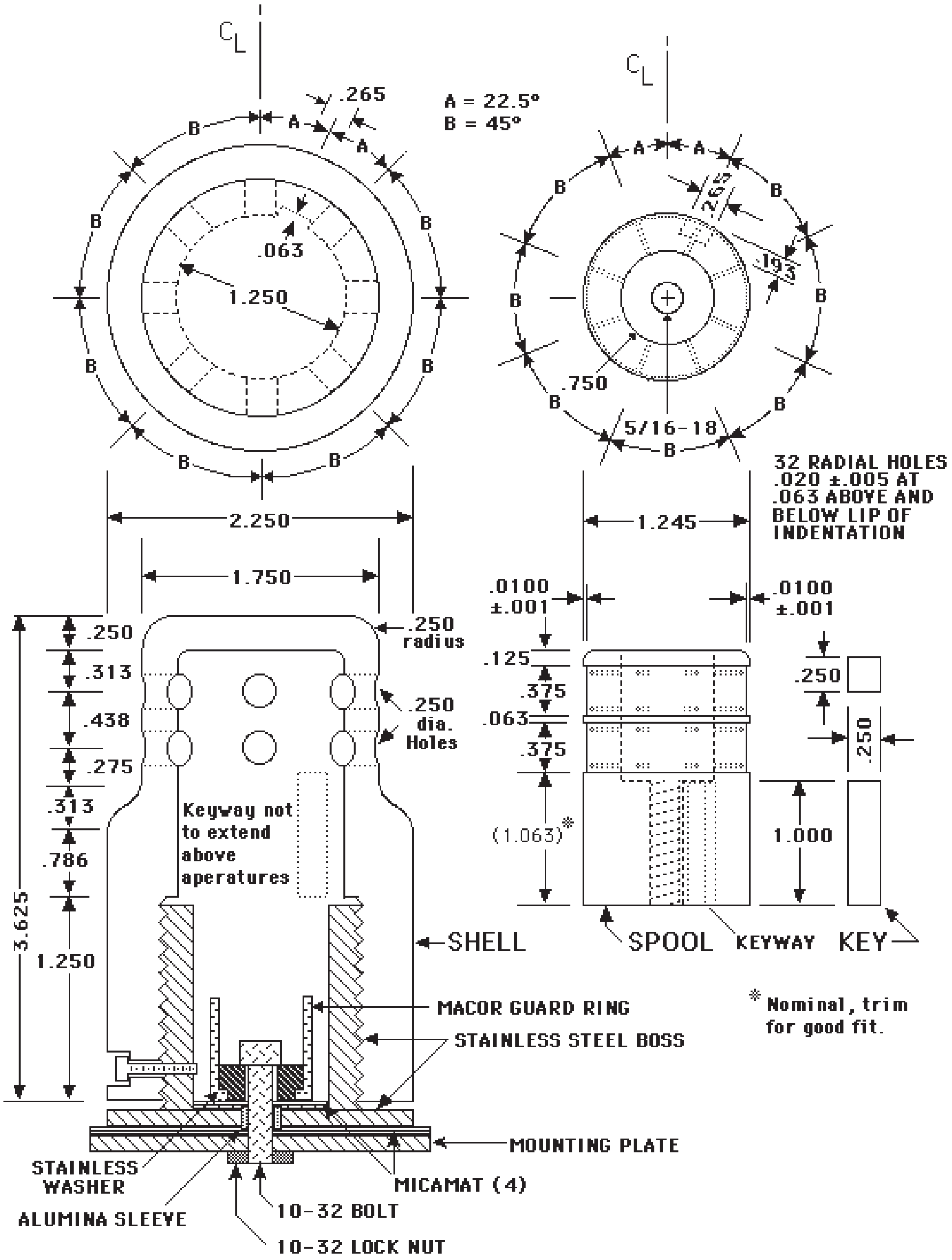

Figure 3.3: *Top and side view schematics of components included in original design of the alpha collector. Dimensions are inches.*

weave carbon-fiber-composite chosen for its superior thermal and structural properties, and made of carbon for its low atomic number (Z). Low Z materials are preferred for use as plasma facing components since the power lost due to Bremsstrahlung radiation is proportional to the effective atomic number of the plasma (Z_{eff}). Z_{eff} increases dramatically if high Z impurities enter the plasma through plasma erosion of wall components.

Two rows of 0.635 cm (1/4 in) diameter collimating ports, for α–particle pitch angle selectivity, are drilled into the 0.635 cm wall of the shell. Each row of collimating ports has eight evenly spaced ports placed 45° apart. The spool is made of graphite and the shell and spool are supported and electrically isolated from the tokamak by the mounting components seen in Fig. 3.2. Two nickel foil stacks are wrapped around the cylindrical spool which is inserted into and keyed to the shell.

The redesign of the probe head shown in Fig. 3.2(b) was prompted by the need to reduce foil heat damage from neutral beam ion loss as will be discussed in Sec. 4.3. The primary change was an extension of the collimating port depth by drilling 0.635 cm holes through the original spool design (labeled as the Collar in Fig. 3.2(b)). This collar is then modified to fit a new smaller spool inside of it. So the original design has ports of 0.635 cm in width (w) and depth (d), whereas the redesign has w =0.635 cm, but has twice the port depth at d = 1.27 cm (1/2 in). These port dimensions allow high energy particles (i.e. $\rho \gg w, d$) with trajectories within ±45° of a port's axis to strike the foils in the original design, but an acceptance range of only $\sim \pm 27°$ for the redesign, which improved the pitch angle resolution.

The choice of nickel as the implantation foil was based on the immobile character of He in Ni at temperatures below $\sim$ 400°C [30, 32]. The Ni foil, acquired from Goodfellow Corporation, has a 99.95% purity rating and a ±10% thickness accuracy as determined by weight. As depicted in Fig. 3.4, a foil stack is prepared by folding a 10 cm$\times$10 cm sheet of 1 μm Ni foil 9 times to form a 10 cm x 1 cm strip consisting of 10 layers. The foil is folded in a 'rolled' fashion, rather than an 'accordion' fashion, to limit the amount of tritium that can diffuse to the inner layers during exposure to a DT plasma. Tritium adhering to the foil surfaces can present a radioactive contamination problem once the foils are removed from the probe. In the event that the outer layers

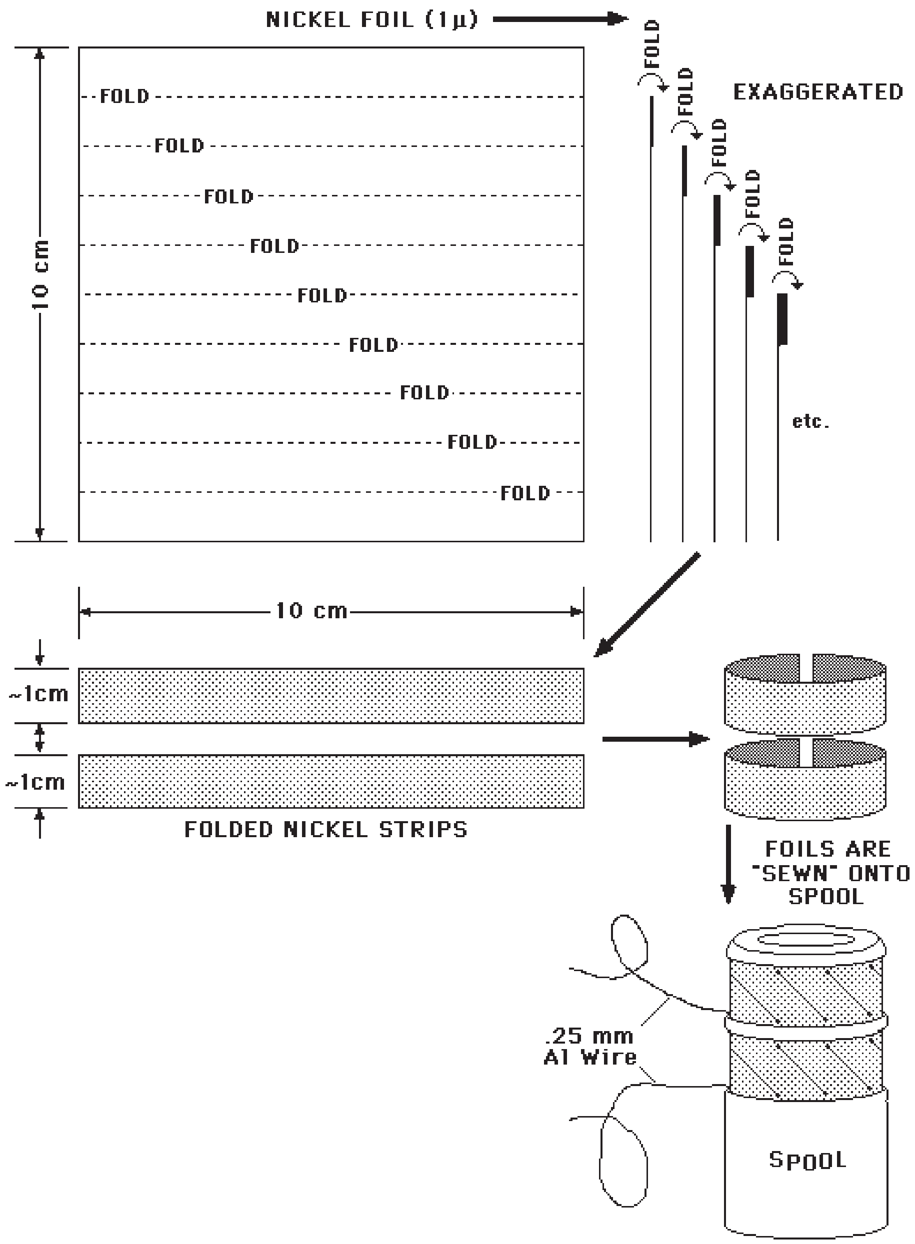

Figure 3.4: *Nickel foils are 'rolled' to produce two 1 cm×10 cm strips of ten layer stacks which are wrapped and 'sewn' onto the spool prior to being inserted into the alpha collector probe head.*

of the rolled stack (layers 1 and 10) are overly contaminated with tritium they can be removed and discarded. The remaining layers can then be surveyed for tritium contamination and decontaminated to acceptable levels (Sec. 3.4.3).

The Ni foil stack is wrapped around and 'sewn' onto the spool using 0.25 mm aluminum wire and the overlapping ends of the Ni are spot welded together. The Al wire holds the Ni tightly to the graphite spool, improving the thermal contact between the Ni and the spool, allowing the spool to act as a heat sink. The 660°C melting point of Al enables the wire to also act as a temperature indicator. If the Al wire exposed in a collimating port experiences any melting due to heat flux from a plasma discharge then it is assumed that the Ni foil in that port exceeded 400° C and the implanted He sample is no longer a reliable indicator of escaping α–particles.

The range of 3.52 MeV birth energy α–particles in Ni is seen in Fig. 3.1 to be 6.0 μm. The standard deviation of the depth distribution, or straggling, is 0.15 μm for alphas at this energy. Removing the first layer results in a lower energy limit of about 0.5 MeV. The collimating effect of the port results in most particles implanting into the foils at near normal incidence. For collimating ports of equal depth and diameter whose dimensions are much less than the gyroradius of an alpha, the straggling of the range distribution is broadened in the direction of reduced depth by $\sim$ 10% due to alphas implanting at less than normal incidence.

The choice of 1 μm Ni foils arranged in a stack and collimating ports of equal depth and diameter should result in the ability to resolve between the first orbit alpha loss at 3.52 MeV, which should be implanted in the sixth and seventh layers of the foil stack, and other losses at energies below about 2.8 MeV, which would be implanted in the fifth and shallower layers. This results in an energy resolution of about $\sim$ 20%, a significant improvement over the $\sim$ 50% resolution of the scintillator detectors [8].

3.4 Sample Analysis

3.4.1 Thermal Desorption Spectrometry

The sample analysis method is based on thermal desorption spectrometry (TDS) using resistive heating of the samples and a UTI 100C residual gas analyzer (RGA), consisting of a quadrapole mass spectrometer with an electron multiplier, for He detection. The sample analysis system was developed and operated at the University of Toronto's Institute for Aerospace Studies in collaboration with PPPL.

The sample analysis vacuum chamber, illustrated in Fig. 3.5, is pumped down to $\sim 10^{-5}$ torr, as measured by the ion gauge, using the combination of a mechanical roughing pump and a turbo pump. A baking jacket is placed over the vacuum chamber and baked at 150°C for 24 hours to drive gases out of the walls and components of the system. This bake also drives deuterium out of the Ni foils which would otherwise corrupt the measurement since deuterium has the same charge to mass ratio as ^{4}He. This bake is conducted at sufficiently low temperature to ensure that the implanted He remains immobile in the Ni.

The system vacuum is improved further to a base pressure of $\sim 10^{-9}$ torr with the aid of a titanium sublimator and a liquid nitrogen cold finger. The titanium sublimator only getters out reactive gases and so has no effect on the He concentration. Most gases are condensed onto the surface of the cold finger, particularly methane which may be present in significant quantities but is not removed by the sublimator. The cold finger also has no effect on the He concentration due to the low boiling point of He. The effectiveness of the bake and titanium sublimator were tested by analyzing a foil sample implanted with $\sim 10^{16}$ deuterium atoms, over 7 orders of magnitude above the minimum sensitivity of the sample analysis system of 5×10^8 atoms. This test resulted in no mass-4 signal being detected by the RGA, meaning the deuterium had been effectively removed.

Each of ten tantalum foil strips is folded in half to form a pocket which holds a Ni foil sample corresponding to a specific collimating port and layer depth. Attached

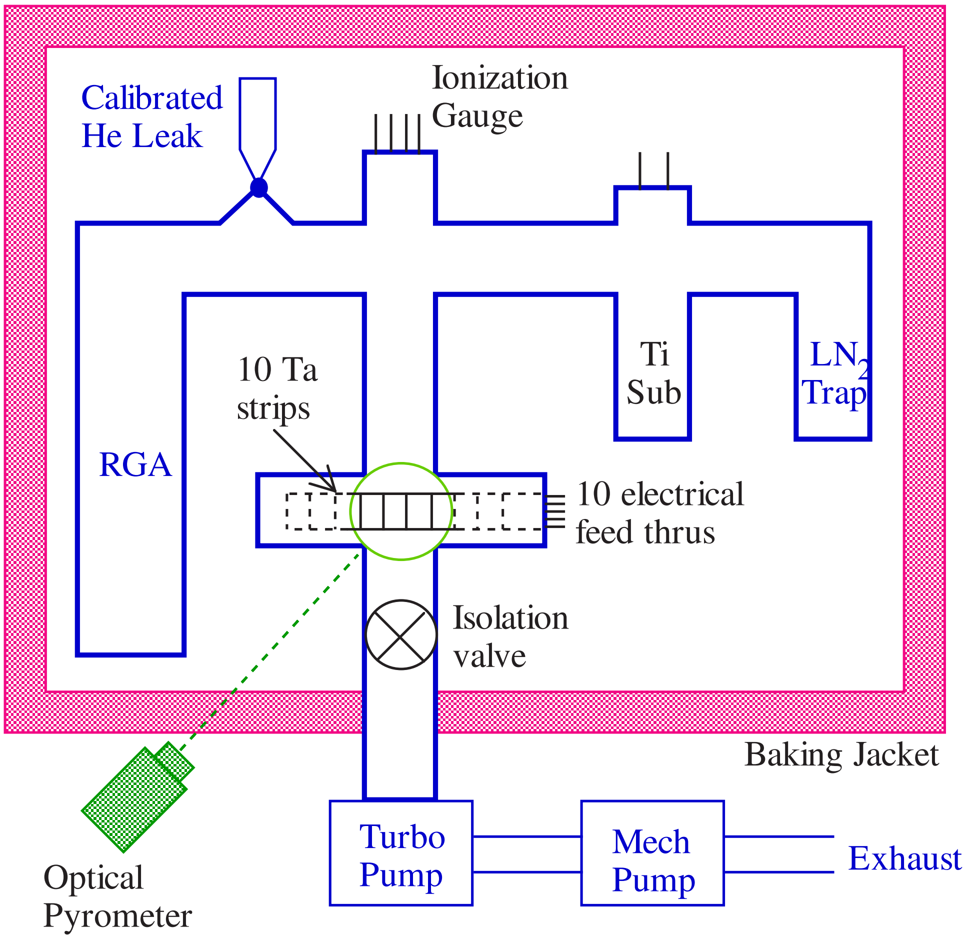

Figure 3.5: *Sample analysis system used to desorb and measure He from nickel samples.*

to one side of each tantalum holder is an electrical lead that penetrates the vacuum vessel through a vacuum sealed electrical feedthrough. The other side of each holder is grounded to the vessel. One at a time, a current of ~30 A is passed through each tantalum holder, resistively heating it to $> 1700°$C as measured with an optical pyrometer viewing the holders through a vacuum window. Nickel, with a melting point of 1453°C, quickly melts releasing the implanted He to the vacuum chamber which has been isolated from the pumps by shutting the isolation valve. The ^{4}He signal of the RGA is then recorded by an interfaced PC. Between each foil analysis the valve is opened to allow the pumps to remove the He in the system from the previous sample. The RGA output is calibrated before and after the analysis by introducing He into the system at a known rate using a calibrated He leak.

TDS was chosen over other surface sample analysis methods for its ability to achieve excellent minimum sensitivity. The system used was capable of detecting He levels as low as 5×10^8 atoms in the ~1 liter vacuum system. By desorbing all the He contained within the 1 μm thick foil, in essence integrating all the He contained within a $\sim 3 \times 10^{-5}$ cm^3 volume, a minimum He concentration of $\sim 2 \times 10^{13}$ atoms cm^{-3} was detectable, roughly two orders of magnitude smaller than expected concentrations based on first orbit loss modeling (Sec. 4.2). By comparison, the secondary-ion mass spectrometry (SIMS) system used to measure ^{3}He and ^{4}He ions heated by ICRH in JET, achieved a sensitivity of only 5×10^{18} atoms cm^{-3} [28], about three orders of magnitude higher than levels expected for alpha collector samples.

Resistive heating of samples was chosen for its simplicity, trading off the ability to process large numbers of samples in a single batch. To ensure good minimum sensitivity, the main concern in choosing a desorption method was minimizing vacuum system volume to be able to maximize the partial pressure of released He. Systems using external heating sources, such as lasers or flash lamps, that could process on the order of 100 samples in one analysis run were considered. However, instead of minimizing vacuum volume by using an external heating source, it was decided to limit the number of samples in a batch to 10 to allow use of a 10 pin electrical feedthrough to provide the resistive heating current.

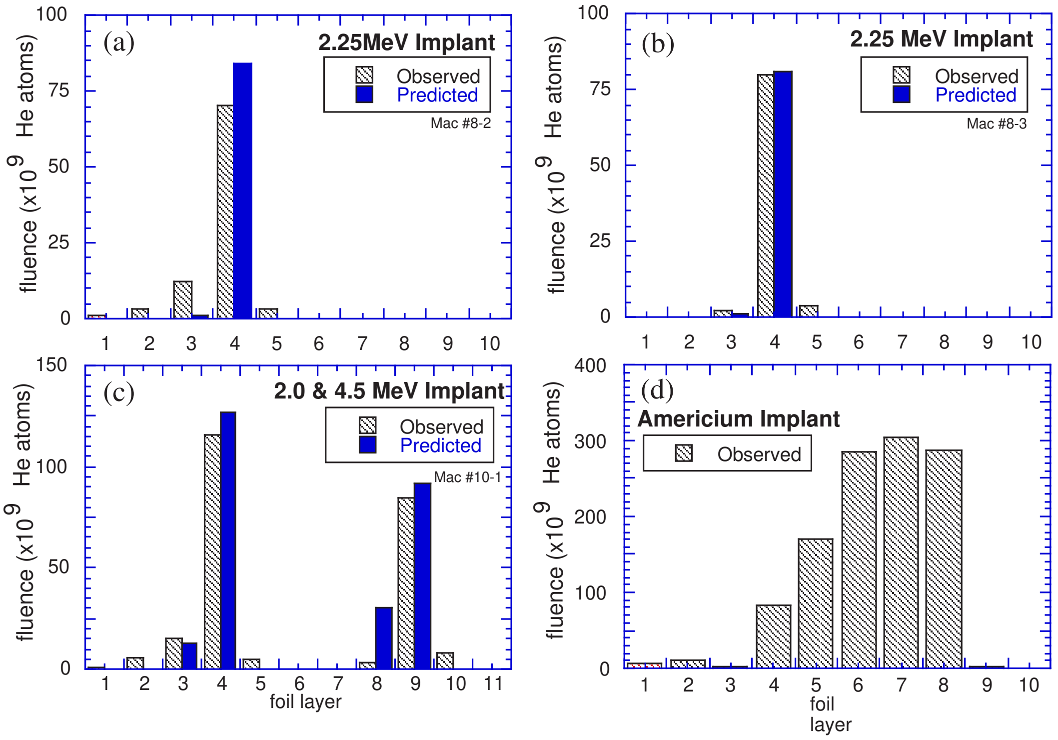

Figure 3.6: *Calibration samples implanted at McMaster University's Van de Graaff accelerator with monoenergetic He beams at (a) and (b) 2.25 MeV; (c) 2.0 and 4.5 MeV; and (d) calibration sample implanted using* ^{241}*Am 4.5 MeV alpha source.*

3.4.2 Absolute Calibration

For use as a check of the absolute calibration of the sample analysis, calibration samples were prepared at McMaster University using a Van de Graaff accelerator [32]. Monoenergetic beams of He ions were implanted at normal incidence into stacks of 1 μm Ni foils. These sample were then analyzed using the method described in Sec. 3.4.1. Figs. 3.6 (a) and (b) show the depth distributions for two Van de Graaff calibration samples at 2.25 MeV. Rutherford backscattering was used to accurately measure the total fluence implanted. IBM's Monte Carlo TRIM-95 code that calculates the penetration of ions into solids (Sec. 4.2.2) was used to calculate the predicted depth distribution. Good agreement was found between the observed and the predicted distribution. Slight spreading of the distribution, such as in Fig. 3.6 (a) was attributed to nonuniformities in the foils. Fig. 3.6 (c) shows acceptable agreement between predicted and observed depth distributions for a single foil sample with two separate implants at 2.0 and 4.5 MeV.

As another check of the absolute calibration, a foil stack was implanted using an Americium-241 alpha source. The source was an Amersham International AMRQ7779 sealed ^{241}Am 4.5 MeV alpha reference source containing 135 μCi of activity which emitted $\sim 10^6$ alphas/min$\cdot\mu$Ci from the face of a 1 cm diameter circular foil. The source was placed over a 0.635 cm deep and 0.635 cm diameter collimator drilled out of an aluminum blank. A stack of ten 1 μm nickel foils was placed flat against the other side of the collimator. The source was left in place for 173 days, yielding a total predicted implanted fluence of $\sim 10^{12}$ alphas, in excellent agreement with the total measured He content of 1.2×10^{12} alphas. Taking into account the geometry of the source and collimator, the energy distribution of the source as a function of emission angle, and energy attenuation in air, the α–particle concentration was expected to peak in the 7th foil layer and to be distributed from the 4th to 8th layers. The measured depth distribution, shown in Fig. 3.6(d), is in good agreement with this prediction. This foil sample underwent the decontamination process described in Sec. 3.4.3 to ensure that the decon process would not interfere with implanted He levels.

3.4.3 Decontamination

Decontamination of the foils was necessary to avoid contaminating the sample analysis vacuum system with tritium that may have adhered to foil surfaces during exposure in TFTR. Initially, water soaked cotton swabs were used to wipe down the foils, but this proved to be insufficient. Several decon methods were considered including cleaning with a surfactant, baking, and ultrasonic bathing. Ontario Hydro Technology's Tritium Lab, having vast experience with tritium contamination, offered use of their decon expertise and facilities. Upon their suggestion, it was decided to bake the foils at 200°C under a flow of wet argon for 24 hours [33, 32]. Destructive testing of foil samples exposed to TFTR's DT environment, but not needed for He analysis, showed that this process removed over 90% of the tritium adhered to the foils. In addition, the first layer, which was found to contain over 90% of the total tritium in a foil stack, was discarded.

The bake at 200° was conducted at low enough temperature to avoid the release of implanted He, which remains immobile below about 400°C. To ensure that the decon process did not cause desorption of He from Ni samples, the ^{241}Am calibration sample (Fig. 3.6(d)) underwent decon prior to being analyzed.

3.5 TFTR Implementation

Fig. 3.7 depicts a poloidal cross section of TFTR showing the exposure position of the alpha collector probe at the bottom of the vessel, and the poloidal projection of the RF limiters. TFTR has nine carbon poloidal RF limiters of varying poloidal extent to protect the RF launchers. They are centered at a major radius of 261 cm and have a minor radius of $99.0 \pm \sim 0.2$ cm.

After exposure to one or more discharges, the probe is lowered remotely and isolated from the TFTR vacuum vessel by shutting the torus interface valve shown in Fig. 3.7. The probe chamber can then be vented and the probe head removed through a six inch flange. The exposed nickel foils are then removed for analysis and replaced with new foils. Also shown in Fig. 3.7 are various α–particle orbits that strike the detector for a 2.45 m major radius plasma with a plasma current of 1.8 MA. These orbits will be discussed in more detail in Sec. 4.2.

Fig. 3.8 is a partial toroidal cross section of TFTR showing the position of the alpha collector with respect to the nearby poloidal RF limiters and the 90° lost alpha scintillator detector. The alpha collector and the lost alpha scintillator detectors are located in adjacent bays separated by one of the 20 toroidal field (TF) coils, placing them 18° apart toroidally. The major radii of the alpha collector probe and the 90° scintillator detector are 262.5 cm and 259.2 cm respectively, placing each of them within 2 cm of the major radius of the RF limiter center.

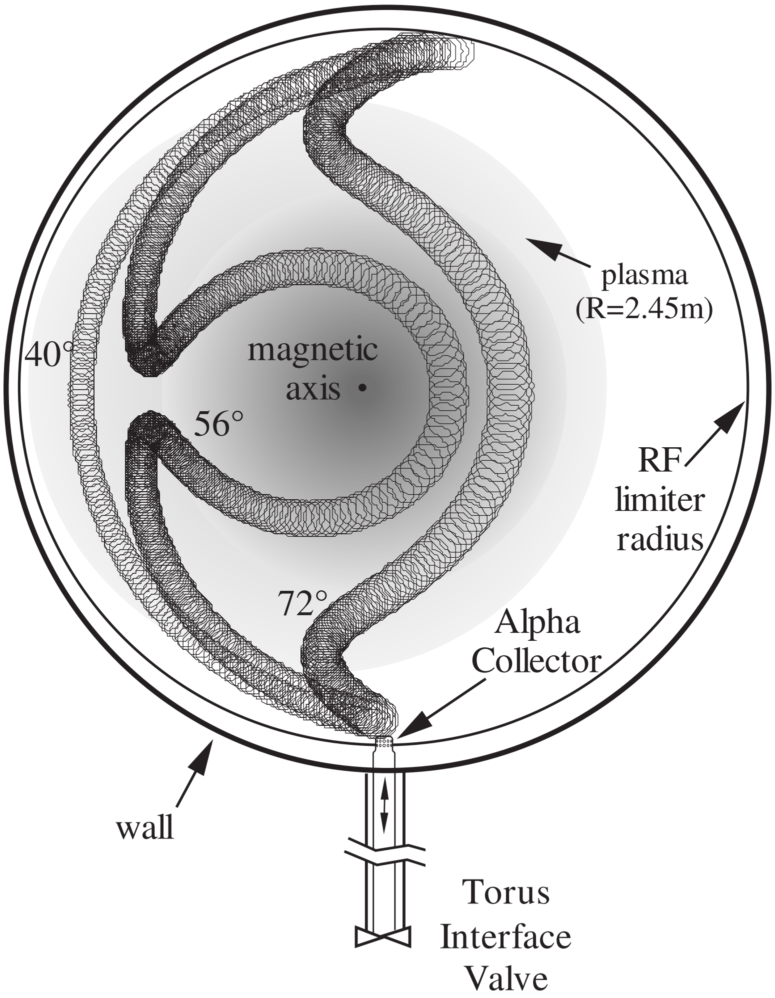

Figure 3.7: *Poloidal cross section of TFTR illustrating a co-going passing particle (χ_t = 40°, where χ_t is the toroidal pitch angle at the detector), a trapped particle at the fattest banana orbit (χ_t = 56°), and a deeply trapped orbit (χ_t = 72°) that strike the alpha collector probe located at the bottom of the vessel for a 1.8 MA plasma. Once exposed, the alpha collector is lowered below the torus interface valve so it can be isolated and removed.*

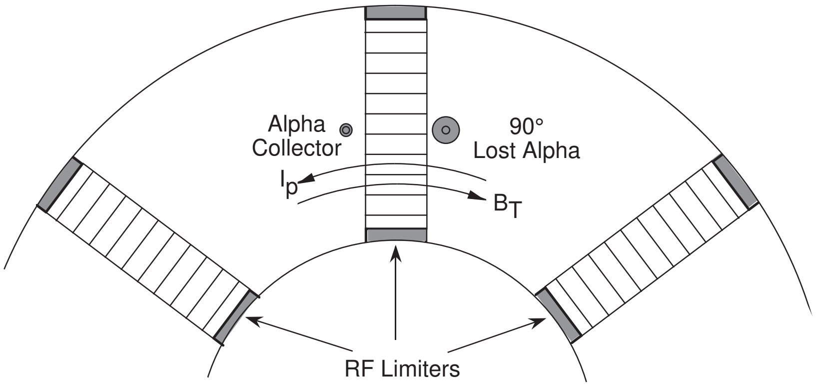

Figure 3.8: *Top view of TFTR vessel showing the relative locations of the alpha collector and the 90° lost alpha scintillator detector with respect to the nearest RF limiters.*

Particles intercepting the 90° lost alpha scintillator detector on co-going (in relation to the plasma current) orbits have 45° of toroidal clearance between the center of the nearest RF limiter and the detector. Particles intercepting the alpha collector on co-going orbits, however, only have 9° of toroidal clearance, making it necessary to position the probe closer to the plasma to avoid shadowing of these orbits by the limiter. This is essential for detection of first orbit loss since the majority of this loss occurs on the co-going leg of trapped banana orbits such as the 56° and 72° orbits depicted in Fig. 3.7. Orbits near the 56° 'fattest banana' dominate first orbit loss because they pass closest to the magnetic axis where the alpha source rate is peaked.

Fig. 3.9 shows the alpha collector and nearest RF limiter as seen when looking toward the center of the torus. This figure depicts a co-going alpha particle orbit entering a collimating port on the detector. Alpha particles can enter any one of a series of 16 collimating ports that are separated into two rows on the cylindrical probe head. At the back of each port is the 10 layer stack of 1 μm thick nickel foils into which the alpha particles implant. Each port only accepts particles within a particular range of pitch angles.

The edge of the probe and the RF limiter are separated toroidally by 12.4 cm.

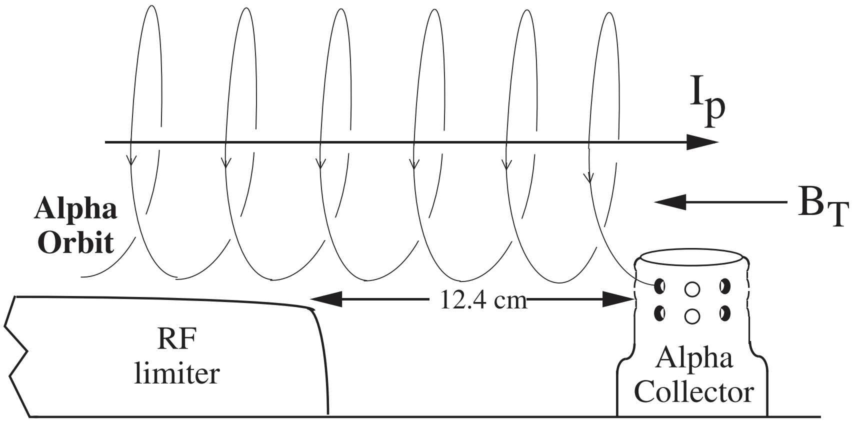

Figure 3.9: *Side view (looking in toward centerline of TFTR) of the alpha collector probe head depicting a co-going alpha particle entering one of the 16 collimating ports.*

The probe was placed in the same position for each exposure, placing the center of the upper row of collimating ports 0.5 cm radially inward from (i.e. above) the nearest limiter, and the lower row 0.6 cm radially outward from (i.e. below) the limiter. This was sufficient to avoid shadowing of first orbit loss at 3.5 MeV to both rows, as will be discussed in Sec. 4.3.4. The top of the lower row of collimating ports was only 0.3 cm below the RF limiter. The larger toroidal separation for co-going orbits between the nearest RF limiter and the 90° scintillator detector allows its 0.1 cm high pinhole aperture to be placed ~1.2 cm below the RF limiter [22], or ~0.9 cm below the top of the lower row of the alpha collector.

A cross section taken through the middle of a row of collimating ports is shown in Fig. 3.10(a) for the original design and Fig. 3.10(b) for the redesigned probe head. The orientation of each port is labeled in Fig. 3.10 with respect to the toroidal direction (0° corresponding to the collection of co-going particles). The redesigned head was rotated with respect to the original probe head by 7.5° clockwise when viewed from above. This was to line the probe head up with the scintillator detector which is oriented along 67.5°. For convenience, the orientations of the original design will be referred to when discussing the probe in general (subtract 7.5° to obtain the redesign orientations).

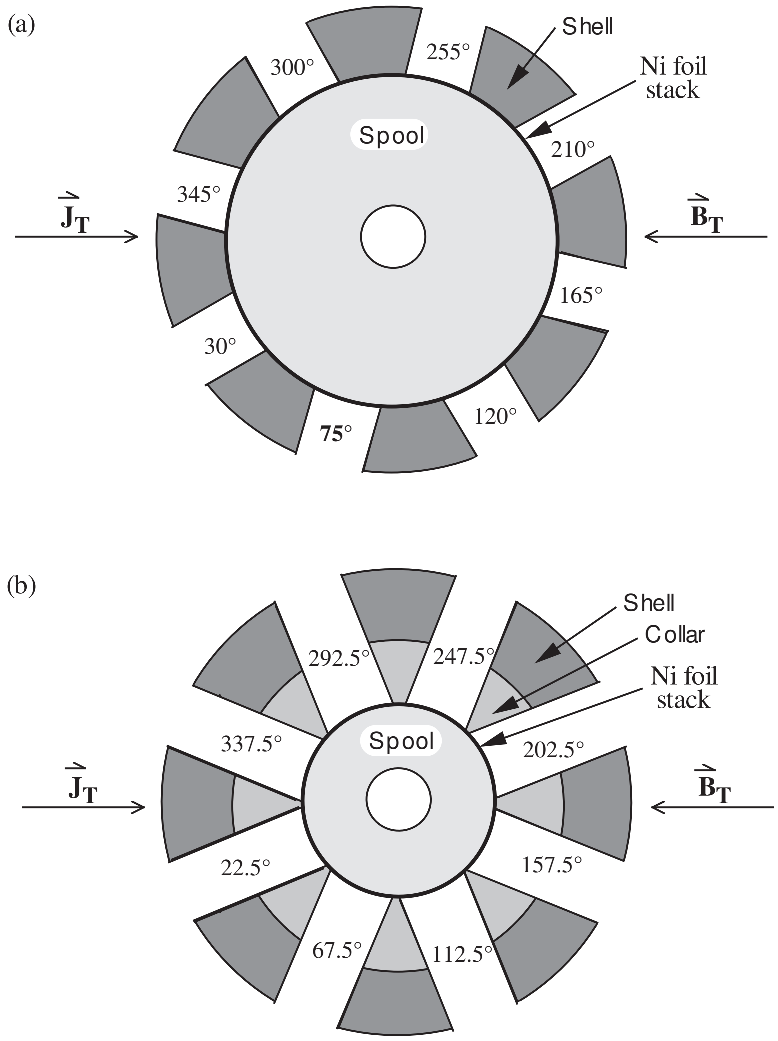

Figure 3.10: *Midplane cross section of a row of collimating ports for the (a) original design and (b) redesigned alpha collector probe head. The stack of 10 layers of 1 μm Ni foil is wrapped onto the inner spool which is then inserted into an outer shell. Cylindrical 0.635 cm diameter holes drilled into the 0.635 cm thick outer shell make up the collimating ports. The collimator depth is extended to 1.27 cm in the redesigned head of (b) by inserting a cylindrical 0.635 cm thick collar that also has 0.635 cm diameter holes drilled into it. The spool diameters are (a) 3.175 cm and (b) 1.905 cm*

Advantages of Alpha Collector:		
	Scintillator	Collector
A1. Energy Resolution	±50%	±20%
A2. Absolute Calibration	~ factor of 2	±15%
A3. DT Noise Immunity	Fair	Good
A4. Positive Ion Identification	No	Yes
A5. Pitch Angle Coverage	40-80°	0-180°
A6. Radial Coverage	No	Yes

Disadvantages of Alpha Collector:		
	Scintillator	Collector
D1. Time Resolution	50μs	1s
D2. Real Time	Yes	No
D3. Access Required	No	Yes
D4. Pitch Angle Resolution	±3°	±45°
D5. Multiple Ion Detection	Yes	He^4, He^3
D6. Passive Detection	Yes	Less passive

Table 3.1: *Comparison of Escaping Alpha Diagnostics*

3.6 Comparison to Lost Alpha Scintillator Detectors

The lost alpha scintillator detectors are described in Sec. 2.5.1. The alpha collector complements the lost alpha scintillator detectors in many ways. Each has its strengths and weaknesses. Table 3.1 summarizes the advantages and disadvantages of the alpha collector as compared with the scintillator detectors. The advantages of the alpha collector are:

A1. As discussed in Sec. 3.3 the alpha collector, in its current configuration, is capable of achieving 20% energy resolution, a significant improvement over the 50% resolution obtainable with the scintillator detectors. Further improvement in the energy resolution may be possible by using thinner Ni foils and higher degrees of collimation. The use of 1/4 μm Ni foils and deeper collimating ports may allow an energy resolution limited by the straggling of the distribution to

$\sim 5\%$.

A2. Absolute calibration of the foil deposition method is inherently straightforward since it is possible to accurately determine the number of alpha particles implanted in the foils by measuring the partial pressure of ^{4}He in a closed volume in which the foils are melted. Due to a combination of several factors, including uncertainties in the light output per MeV ion, in the angular distribution of this light output, and in the optical throughput of the lenses and fiber bundles, the absolute calibration of the scintillator detectors for DT is uncertain by about a factor of ~ 2 [34]. Thus the foil deposition method should provide a valuable absolutely calibrated cross-check with these detectors and a means of validating alpha loss models.

A3. Since there are no optics nor electronics that can experience interference or degradation from high neutron fluxes, the foil deposition technique may prove more survivable than other detection methods in ITER and future DT reactors. Extensive efforts went into shielding the fiber optics, detectors (CCDs and PMTs) and associated electronics of the scintillator detectors on TFTR, resulting in a signal-to-background ratio slightly above unity [22]. It is not clear whether scintillator detectors can be designed to provide useful alpha loss information in the harsh neutron environment of a DT reactor such as ITER.

A4. The use of an RGA allows the positive identification of different ion species by means of mass spectrometry. Thus the sample analysis of the foil deposition method is capable of distinguishing between ^{4}He signals and those of the D-D fusion products, 3 MeV protons and 1 MeV tritons. Deuterium, which has the same charge to mass ratio as ^{4}He, but is not as immobile in Ni as He, is driven off the foils by the decontamination process and the low temperature bake ($< 200°$C) so as not to be counted as He. The scintillator detectors, on the other hand, are unable to discriminate between high energy ions, leading to ambiguity when fusion products and other high energy ions exist in comparable quantities (e.g. during ICRH minority heating experiments).

A5. The alpha collector was designed to collect alphas over the full pitch angle range of 0–180°, with the exception of a small region ($\approx 8°$) around 90°. Alphas with a pitch angle $\approx 90°$ are shadowed by the probe head itself, making detection of ripple well trapped particles (Sec. 4.5) unlikely. The scintillator detectors were designed such that they only cover $\sim$40–80° in pitch angle, possibly missing important alpha loss features.

A6. The alpha collector was designed with two rows of collimating ports to provide radial dependence information of alpha loss. Also, being mounted on a movable probe enables a scan of radial position. The scintillator detectors contain only one collimating aperture, and, with the exception of the 20° detector, are mounted in a fixed position behind the RF limiter radius.

The advantages over the scintillator detectors made possible by the specific design of the foil deposition alpha collector (A1, A5 and A6) make it a particularly useful complementary escaping alpha diagnostic for TFTR. While some of the advantages can be lost through possible design changes of the scintillator detectors, advantages A2, A3 and A4 are inherent advantages of the alpha collector that may prove valuable in future DT reactors. Of course, there are also inherent disadvantages to the foil deposition detection method:

D1. The time resolution of this technique is inherently poor. The current detector foils must be exposed to a minimum of one TFTR shot, resulting in a time resolution on the order of one second. In a reactor operating in steady state it may be possible to design fast acting shutters over the collimators or moving foil samples at the back of collimators. The time resolution will be limited by the exposure time necessary to obtain a signal greater than the minimum sensitivity of the sample analysis. JET is attempting a similar foil stack diagnostic in which each of several electrically insulated layers are monitored in real time for charge collection, essentially making a stack of Faraday cups [35]. It may prove too difficult to overcome DT neutron electronic interference of a DT reactor with such a method, but if successful, it could overcome the next two disadvantages as well.

D2. A large turn around time is required to remove the foil samples from the tokamak and to analyze them. With the current probe, it is possible to change out foils overnight in preparation for new exposures the next day. The process of shipping, decontaminating and analyzing the foils in Toronto limits the time to availability of data to a few weeks. While vast improvements are possible it is difficult to imagine a real time diagnostic using this technique.

D3. Removing and replacing the foils requires access to the TFTR test cell basement during machine down time to open a tritium contaminated system. A remote sample retrieval system allowing foil replacement during machine operations would be useful for ITER, but tritium contamination remains an issue.

D4. Pitch angle resolution of the alpha collector is determined by the geometry of the collimating ports, with deeper/narrower ports giving better resolution. In the current design, pitch angle resolution was traded off for total α–particle fluence to ensure measurable levels of He in the foil samples. As discussed in Sec. 3.3, the original design has a pitch angle acceptance range of $\pm 45°$, while the redesign has $\pm 27°$. This ensures overlapping coverage between adjacent ports which are separated by 45°. The pitch angle resolution is generally limited by this 45° spacing, although some tricks to get around this are discussed in Sec. 4.3.3.

D5. Advantage A4 can also be viewed as a disadvantage. Since the foil deposition technique is only sensitive to He species, the alpha collector can not be used to diagnose the loss of other high energy ions. Although the lack of ion identification associated with the scintillator detectors can be confusing, it can also be extremely useful if ambiguities can be resolved through a physical understanding of the processes involved.

D6. The fixed scintillator detectors are completely passive, able to diagnose high energy ion losses in any type of discharge without having any effect on the plasma. The alpha collector (and the 20° scintillator detector) is on a movable probe which requires close attention to ensure the probe is not placed to close to the plasma. Thermal damage to the probe head during plasma operations could be catastrophic for TFTR. For this reason, thorough thermal analysis of the probe head was conducted. This thermal analysis allowed operation of the alpha collector just inside the RF limiter radius in disruption free plasmas with major radii as large as 2.52 m. Therefore, the discharges for which the alpha collector was to be used had to be carefully selected. Thermal safety considerations also ensure that the probe head is not far enough into the vessel to have an effect on the plasma.

Modeling and results of the alpha collector are presented in the next chapter.

Chapter 4

Alpha Collector - Modelling and Results

4.1 Introduction

The design of the alpha collector was considered in Chapter 3. This chapter will evaluate the results obtained using the alpha collector in several TFTR DT discharges. First, modeling of the detector response to first orbit loss is discussed in Sec. 4.2. The results of five separate DT exposures are presented in Sec. 4.3 with comparisons to the first orbit model and the results obtained with the lost alpha scintillator detector located at 90° below the outer midplane. These results show that the alpha collector detects a large partially thermalized anomalous loss at the higher plasma current (1.8 MA) which does not appear on the 90° scintillator detector, while the results at the lower plasma current (1.0 MA) are mainly consistent with first orbit loss. In the discussion of Sec. 4.4, the experimental results are summarized and the 1.8 MA anomalous loss is found to be consistent with an anomalous loss feature known as 'delayed' loss which only appeared in DD plasmas on the 90° scintillator detector. A look at the trajectories of α–particles reveals a dilemma regarding radial diffusion to the bottom of the vessel which makes it difficult to explain both 'delayed' loss to the 90° scintillator detector and the 1.8 MA anomalous loss to the alpha collector. Several loss mechanisms are considered in Sec. 4.5, but none provide a satisfactory explanation for the anomalous loss. Summary, conclusions, and suggestions for future work are offered in Chapter 6.

4.2 First Orbit Loss Model

4.2.1 Pitch Angle Distribution

First orbit loss can be calculated using the PPPL Lorentz ORBIT code [36]. The Lorentz ORBIT code integrates the Lorentz force equation to trace a single charged particle's trajectory. Fig. 3.7 shows some typical orbits at various pitch angles that strike the alpha collector. The orbit at a pitch angle of 40° is a co-going passing orbit, whereas the other two orbits are trapped orbits. The orbit at a pitch angle of 56° corresponds to the fattest banana orbit (i.e. at the passing-trapped boundary) and passes closest to the magnetic axis where the alpha source profile is peaked, thus giving the largest contribution to first orbit loss.

By integrating the source profile along particle orbits backwards in time from the detector through the plasma and taking into account the detector area and solid angle, the code calculates the expected collection fraction (alphas/neutron) and pitch angle distribution of first orbit loss striking the detector. The collection fraction is simply the fraction of the total alpha production (equal to neutron production) that is collected by a foil stack inside one of the collimating ports, and can be of the order of 10^{-6} alphas/neutron as calculated by ORBIT.

This collection fraction can be estimated by multiplying the expected global first orbit loss fraction by the ratio of the area of the exposed foil in the detector to the area of the vessel wall that α–particles strike . For a $\sim$10% global first orbit loss spread approximately evenly over the bottom $\sim$1/3 of the $\sim$100 m^2 vessel wall (ion ∇B drift direction is down) it would be expected that an area the size of the exposed foil surface of $\sim 3 \times 10^{-5}$ m^2 would collect $\sim 1 \times 10^{-7}$ of the lost alphas. However, since the foils are perpendicular to the wall they intercept particles that would have struck the wall over a larger area than the foil area, giving the foils a projected area onto the wall about an order of magnitude larger than their geometrical area. This raises the estimate based on the detector to wall area to $\sim 10^{-6}$ alphas/neutron, consistent with the code results.

ORBIT was used to predict the alpha collection fractions for the exposure conditions which will be described in Sec. 4.3. These exposures consist of two shots at 1.0 MA (exposures C & E) and two at 1.8 MA (exposures B & D). Fig. 4.1 is a plot of the predicted alpha collection fraction for first orbit loss as a function of collimating port orientation for the 1.8 MA exposures calculated using the Lorentz ORBIT code. The squares on the exposure B prediction mark the port orientations of the original probe head design which was used for this shot (Fig. 3.10). Likewise, the circles on the exposure D prediction mark the port orientations of the redesigned probe head. The alpha collection fraction is the detector response to the local pitch

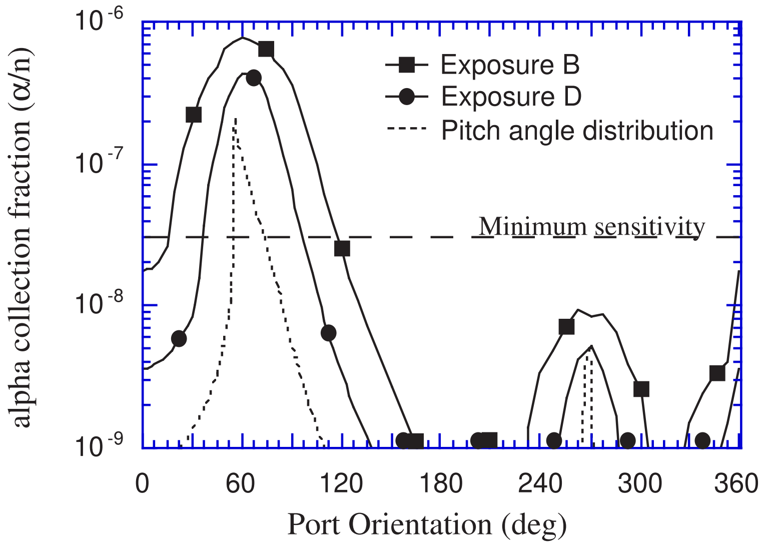

Figure 4.1: *Predicted alpha collection fraction (alphas/neutron) as a function of port orientation for the 1.8 MA exposures using the original (exposure B) and the redesigned probe head (exposure D). The dashed curve represents the expected pitch angle distribution in arbitrary units. The horizontal dashed line at* 3×10^{-8} *alphas/neutron represents the minimum sensitivity assuming* 1×10^{17} *global neutron production.*

angle distribution of the expected first orbit loss, which is plotted in arbitrary units (dashed curve) for comparison. The peaks of the detector response curves (B & D) are shifted to higher pitch angle with respect to the local pitch angle distribution due to the asymmetry in this distribution (i.e. the high pitch angle tail). The reduced magnitude (by ~45% at the 60° peak) of the exposure D curve with respect to the exposure B curve in Fig. 4.1 is the result of reduced alpha collection associated with the deeper collimating ports of the redesigned head.

Since the α–particles of interest have gyroradii much larger than the dimensions of the collimating port ($\rho \approx 5.0$ cm$\gg$ 0.64 cm$= w$), their paths inside the port can essentially be thought of as straight lines. Thus an α–particle striking the foil surface in the original probe head design, in which the port's depth (d) and width (w) are equal (0.635 cm), can have a maximum angle of incidence, $\alpha_{max} = \tan^{-1}(w/d)$, of 45°. This maximum angle of incidence translates to a ±45° pitch angle acceptance range about the orientation of the collimating port axis. The maximum angle of incidence for the redesigned head, in which $d = 2w$, is 26.6°. The FWHM of the detector response curves in Fig. 4.1 can be shown to be approximately the FWHM of the local pitch angle distribution ($\sim 5°$) plus half of the pitch angle acceptance range of the collimating port used in each design (45° for the original head; $\sim 27°$ for the redesign).

The detector response for inboard facing (towards the centerline of the torus, i.e. 180–360°) ports in Fig. 4.1 lies below the minimum sensitivity, illustrated by the horizontal dashed line, estimated for a 1×10^{17} total neutron production (for increased neutron production, the minimum sensitivity in alpha collection fraction is reduced). This is because an α–particle undergoing left handed gyromotion about the magnetic field (Fig. 3.9) must approach the probe head from beneath in order to enter an inboard port and is thus much more likely to be scraped off by the RF limiter before reaching the probe. Only particles with a pitch angle very close to 90° can intercept the inboard side of the detector since they travel nearly straight down (e.g. ripple well trapped particles) and can avoid limiter scrape off. These particles are represented by the peaks centered at the 270° port position. However, these particles would most likely be shadowed by the probe head itself before they could enter a collimating port, an effect that is not taken into account in this simulation. Thus, it is expected that inboard facing ports would not collect significant quantities of escaping alphas.

Since an α–particle is produced for each neutron, the calculated collection fraction is converted to expected alpha fluence by multiplying by the global neutron production. The code's accuracy is highly dependent on the assumed source and current profiles as is discussed in Sec. 4.3.5. These profiles are generally obtained from the transport code, TRANSP [16], which takes inputs from various diagnostics to generate time dependent plasma parameters.

4.2.2 Range Distribution

The Lorentz ORBIT code predicts the total fluence and pitch angle distribution to a detector. However, to determine the range distribution of alphas in the nickel foils it is also necessary to determine the angle of incidence distribution of alphas on the foils. The conversion from pitch angle distribution to incident angle distribution is accomplished using an auxiliary code called PORT, developed specifically for this detector. PORT launches ions backwards in time from a grid on the foil surface of each port at various pitch angles and gyrophases, weighted by the ORBIT-calculated pitch angle distribution. Particle drifts, such as ∇B and curvature drift, are ignored since the particles are generally tracked for less than one gyro-orbit to determine if they clear the probe head. Thus a particle orbit is a simple helix about the magnetic field vector, defined by the particle's gyroradius ρ and pitch angle, $\chi = \cos^{-1}(v_{||}/v)$, where v is the particle's velocity and $v_{||}$ is the parallel velocity component along the magnetic field. The magnetic field at the probe location (i.e. at the bottom of the vessel) is assumed to lie in the horizontal plane (i.e. parallel to the midplane) and to make an angle χ_{bt} with the toroidal direction determined by $\chi_{bt} = \tan^{-1}(B_p/B_t)$, where B_p is the poloidal field and B_t is the toroidal field at the alpha collector. PORT assumes that the first orbit loss to a detector port is independent of gyrophase at the detector (good to within ~20% as determined by ORBIT) and that the foil surface is flat. If a particle clears the port walls and the probe head, it is counted and its angle of incidence is determined. The angle of incidence, α ($0°$ corresponding to normal incidence), is determined by taking the scalar product between the particle's velocity vector at the foil surface and a unit vector along the axis of the collimating port and is found to be:

$$\cos\alpha = \cos\chi \ \cos\chi_0 + \sin\chi \ \sin\chi_0 \ \cos\gamma \tag{4.1}$$

where χ is the particle's local pitch angle ($0°$ being along the magnetic field in the direction of the plasma current), χ_0 is the angle between the magnetic field and the axis of the collimating port, and γ is the gyrophase of the particle at the foil ($0°$ corresponding to the bottom of a gyro-orbit). Fig. 4.2 shows the conversion of 1.0 MA and 1.8 MA ORBIT calculated pitch angle distributions for 3.5 MeV α–particles to incident angle distributions for a $30°$ and a $75°$ port using PORT. Notice that the 1.8 MA pitch angle distribution of Fig. 4.2(a) has a peak at $56°$ corresponding to the fattest banana orbit, which was depicted in Fig. 3.7, since it passes closest to the magnetic axis where the source profile is peaked.

Once the distribution of incident angles onto the foil is determined using the PORT code, the range distribution of 3.5 MeV first orbit lost α–particles can be determined using IBM's TRIM-95 code [37]. The TRIM code uses a Monte Carlo algorithm to

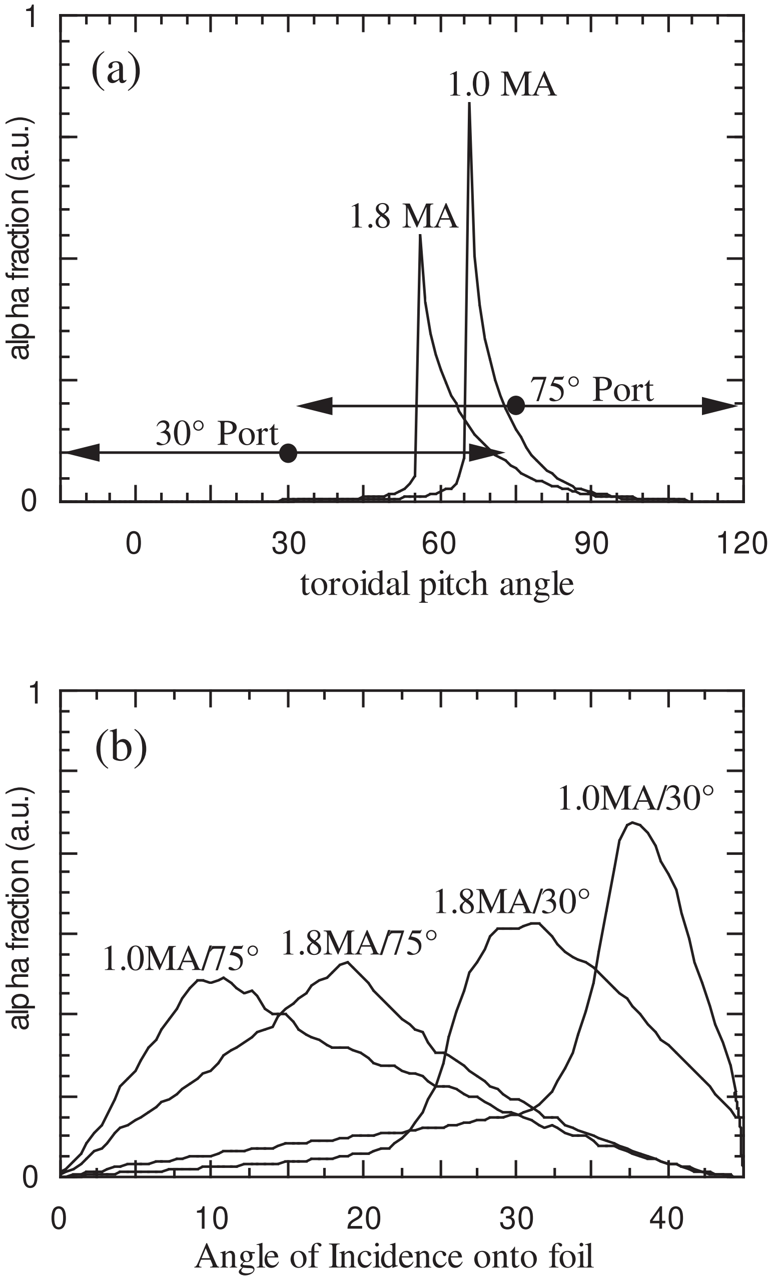

Figure 4.2: *(a) Toroidal pitch angle distributions in arbitrary units calculated by the Lorentz ORBIT code for 3.5 MeV α–particles from exposures B (1.8 MA) and C (1.0 MA). The $\pm 45°$ acceptance range of the original probe design is depicted for the 30° and 75° ports. (b) The resulting angle of incidence distributions for the 30° and 75° ports calculated by PORT for the pitch angle distributions shown in (a).*

calculate the penetration of ions into solids. Fig. 4.3(a) shows the TRIM calculated range distributions for He ions implanted at various energies into nickel at normal incidence. The standard deviation of the range distribution, known as straggling, is ~0.2 μm at 3.5 MeV. The relative magnitude of the distribution peaks decrease with increasing energy as the straggling increases, keeping the area under each curve constant. Discarding the first layer, to minimize tritium contamination, results in a minimum detection energy of ~0.5 MeV.

Fig. 4.3(b) shows the TRIM calculated range distributions for He ions at 3.5 MeV into nickel at various angles of incidence. The widths of the range distributions increase with incident angle because transverse straggling is more significant than longitudinal straggling. These distributions are combined with the predicted incident angle distributions to obtain the expected range distribution for first orbit loss in each nickel foil stack.

The foils are actually curved since they are wrapped around a cylindrical spool inside the probe head. This curvature can cause particles to strike the foil at larger incident angles than if the foil were flat, resulting in a more shallow implantation range. However, this curvature can only be responsible for spreading of the first orbit loss range distribution to, at most, one foil layer shallower. It has little effect on the position of the peak in the range distribution. This effect is neglected along with other spreading effects such as non-uniformities in foil thickness, which may be responsible for the spreading of calibration sample results seen Sec. 3.4.2, and the $\pm \sim$0.5 MeV Doppler broadening of the birth energy distribution (Sec. 2.3.1). These effects taken together can be expected to spread the depth distributions of first orbit loss by one foil layer in either direction.

In the next section, the first orbit loss model predictions generated through the use of ORBIT, PORT and TRIM are compared to alpha collector measurements.

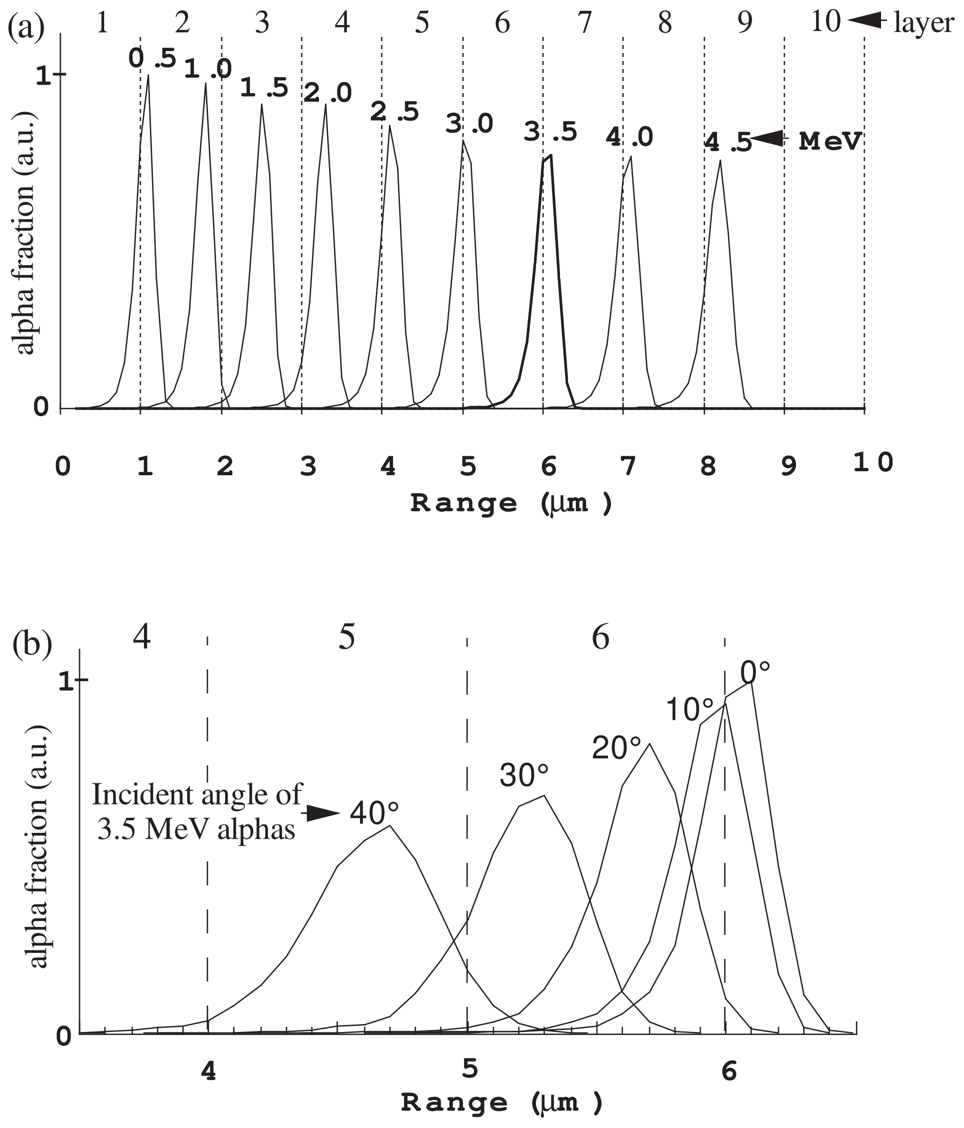

Figure 4.3: *(a) Implantation range distributions for monoenergetic alpha particles implanted into nickel at various energies and at normal incidence as calculated by the TRIM-95 code. The boundaries between the 1 μm thick foil layers are depicted by the dashed lines. (b) Implantation range distributions for 3.5 MeV alpha particles implanted into nickel at various angles of incidence.*

Exposure	A	B	C	D	E
Probe head	Original	Original	Original	Redesign	Redesign
Shot #	73319/73320	74796	76014	80553	84593
I_p (MA)	0.6	1.8	1.0	1.8	1.0
R_0 (m)	2.45	2.45	2.45	2.45	2.45
B_t (Tesla)	4.75	4.75	4.88	4.87	4.88
P_b (MW)	5.2	10.2	9.4	12.7	11.1
t_b (s)	3.0-3.7	3.0-3.7	3.0-3.7	3.0-4.0	3.0-3.7
S_n (x10^{17} n)	0.6	1.3	1.1	4.3	1.8
n_{e0} (x10^{13} cm^{-3})	---	4.6	3.1	4.2	3.6
T_{e0} (keV)	---	6.1	5.8	7.4	6.4
τ_{sd0} (s)	---	0.21	0.29	0.30	0.28

Table 4.1: *Alpha Collector Discharge Parameter List*

4.3 Experimental Results

The alpha collector has been exposed to a total of five DT discharges. Plasma parameters for these 5 discharges, labeled A through E, are given in Table 4.1. These discharges were conducted at low neutral beam injection (NBI) power to avoid MHD activity, so that first orbit loss was expected to be the dominant loss mechanism. The power was also kept low to avoid probe overheating, although thermal design considerations do allow its use in high power discharges with plasmas as large as R=2.52 m. The probe was placed in the same position for each exposure, placing the center of the upper row of collimating ports 0.5 cm radially inward from (i.e. above) the nearest limiter, and the lower row 0.6 cm radially outward from (i.e. below) the limiter. In this position, the probe tip was $\sim$ 16 cm outside the last closed flux surface.

Exposure A

Exposure A was actually exposed to two identical DT discharges (and two 'dry run' DD discharges) conducted at a plasma current of 0.6 MA and a neutral beam power of 5 MW using one co-going (in relation to the plasma current) tritium beam and one counter-going deuterium beam. This exposure resulted in the unexpected melting of a majority of the foils and aluminum wires. It is suspected that neutral beam ion loss was responsible for the overheating of the foils, as explained below. The exposure A foils were not analyzed for He content for this reason.

Although exposure A did not provide useful data in terms of a depth profile of He, the resulting heating pattern did provide useful information. The observation that most of the heat damage occurred in ports that were outboard facing implies that the damage was caused by high energy ions. This is because a large gyroradius is necessary to avoid collimation at these large pitch angles (e.g. 75°). In order to enter an outboard facing port, an ion (which undergoes left handed helical motion w.r.t. the magnetic field) must enter the port on the bottom portion of its gyrophase (Fig. 3.9). Thus its gyrocenter will be above the port. To enter an inboard facing port, however, the gyrocenter must be below the elevation of the port, increasing the likelihood that it would have been scraped off by limiters or other obstructions prior to reaching the port (Sec. 4.2.1). For this reason the foils of the inboard facing ports are not expected to be exposed to a large ion flux, and hence, experienced little damage.

Melting of nickel from room temperature requires heating to the melting point of 1453°K and then additional heating to incur the phase transition. The specific heat of nickel in the temperature range of interest is ≈ 0.5 J/°K·g, and the latent heat of vaporization is 6378 J/g. The minimum heat flux (i.e. ignoring thermal conduction and radiation) necessary to melt 1 μm thick Ni foil with a density of 8.9 g/cm^3 in 1 s is $\approx$6 W/cm^2, with $\sim$ 90% of this energy going into the phase transition. The maximum α–particle heat flux to the foil stack in the collimating port oriented 75° outboard of the toroidal direction for this exposure as predicted by ORBIT is only $\approx$300 mW/cm^2. Thus the expected alpha heating is at least a factor of 20 too small to cause any melting. The peak DT neutron rate for these shots of 6×10^{16} n/s corresponds to a maximum alpha power of 34 kW. Assuming for the moment that the same fraction of the 5 MW of NBI power strikes the 75° foil stack as does the alpha power results in $\sim$ 44 W/cm^2 of beam ion heating to the foils. Thus the large NBI power, combined with the possibility of higher relative NBI ion loss to the probe due to their nonisotropic velocity distribution, may account for the overheating of the foils.

As a means of avoiding heat damage due to excessive NBI ion loss, subsequent exposures were conducted at higher plasma current and used co-going only NBI. The effect of the higher plasma current is to reduce the banana width of trapped beam ions allowing more of them to be confined. The use of co-going beams also causes more trapped beam ions to be confined since they are ionized on the co-going leg of their banana orbits and move in closer to the center of the plasma on the subsequent counter-going leg. The use of counter-going beams has the opposite effect of neutrals ionizing on their counter-going leg and then shifting outward during their co-going leg and thus are more likely to be unconfined. The result that calculated prompt first orbit loss of neutral beam ions ranges from 30 to 38% (depending on the beam tangency radius) for counter-injection, and only 0 to 1% for co-injection, for a 2.6 m major radius plasma at a plasma current of 0.9 MA [13] illustrates the strong dependence of beam ion loss on the direction of beam injection. These two modifications, namely higher plasma current and co-going beams, resulted in virtually no overheating of the foils in subsequent exposures with the exception of two ports which were facing directly into the magnetic field and presumably were exposed to excessive thermal plasma flux. None of the exposed Al wires experienced any melting.

NBI ions were not taken into consideration in the original design of the collimating ports. Their relatively large gyroradius of about 1.6 cm for 100 keV tritium ions allows a large fraction of them to reach the foils without being separated out by collimation. The PORT code was used to calculate the fraction of high energy ions with a given gyroradius that can avoid collimation to reach the foils. Fig. 4.4 shows the fraction of ions that can reach the 75° foils without being separated out versus the collimating port depth. A port width of 1/4 in (0.63 cm) and a flat pitch angle distribution were assumed and the gyrophases of the particles were incremented from -90° to 90°, 0° being the bottom of a gyro-orbit. The maximum transmission is calculated for particles hitting the foil at the pitch angle corresponding to the orientation of the port (i.e. 75°). It can be seen from Fig. 4.4 that the original design depth of 1/4 in did little to discriminate between alphas and the smaller gyroradius NBI tritons. By increasing the port depth the collimator is made much more effective in discriminating between the two ion species. For this reason the redesigned probe head was developed

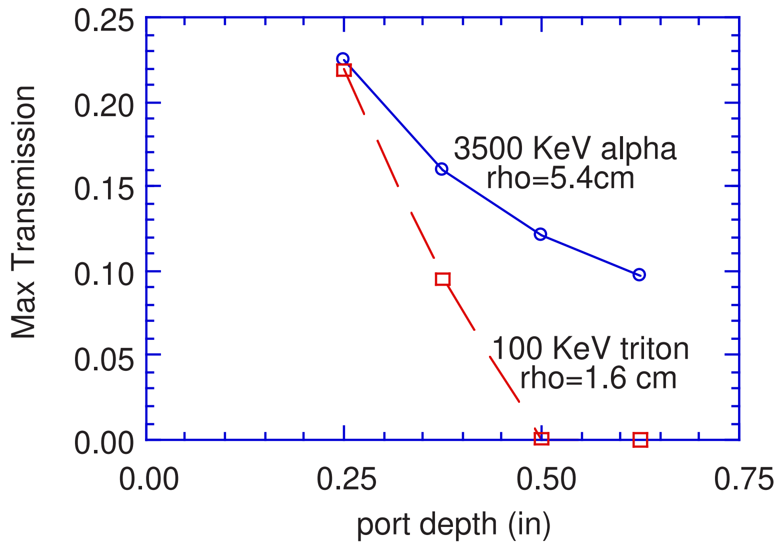

Figure 4.4: *Maximum transmission fraction for* $\chi = 75°$ *particles hitting the 75° foil stack versus collimating port depth plotted for birth energy alphas and NBI tritons. Averaged over gyrophase* $(-\pi/2$ *to* $\pi/2)$ *and foil surface for 1/4 in diameter port. NBI transmission cuts off at* $d = 1/2$ *in.*

with ports having double the depth at 1/2 in (1.27 cm) while leaving the diameter at 1/4 in. As can be seen in Fig. 4.4, this has the effect of nearly eliminating the ability of NBI ions to reach the foils in this 75° outboard facing port, while only reducing the maximum transmission of alpha particles by about a factor of 2. This, combined with a reduced pitch angle acceptance range of also about a factor of 2, results in reducing the alpha flux by only about a factor of 4 for the 75° port when compared to the original design (assuming a flat pitch angle distribution). The redesigned probe head allows the use of the alpha collector in discharges with low plasma current and/or counter-going beams (such as exposure A), but it has not been exposed in TFTR under these conditions.

Exposures B–E

Exposures B through E are nominally identical discharges with the exception of the two values of plasma current and slight modifications that can be seen in Table 4.1.

Note that exposures B & C used the original probe head, and exposures D & E used the redesigned head with collimating ports that were twice as deep, and the head rotated clockwise 7.5° (Sec. 3.5).

Exposures B through E suffered only minimal foil heat damage, and only in ports that had a direct line of sight along the magnetic field on the side opposite the nearest RF limiter. This corresponds to ports at 165° and 210°. Thermal plasma could flow along field lines unimpeded to the foils in these ports. These four samples (i.e. the upper and lower row of the 165° and 210° ports) were not analyzed for this reason.

Analysis of foils from the inboard facing ports (towards the center of the torus) resulted in levels of implanted He below or near the minimum sensitivity ($\sim 5 \times 10^8$ alphas). This was as expected for the reasons discussed in Sec. 4.2.1. Therefore, only the outboard facing ports are compared to the first orbit loss model in this section. Although there was essentially no He implanted in these inboard facing samples, it was important to obtain these results to verify expectations and to provide additional insight into any anomalous results that may be obtained.

When a fluence measurement is compared to the first orbit loss model in this section, only the summed fluence of foil layers 4 through 9 is included. Due to the geometry of the collimating ports and the predicted range distribution of 3.5 MeV α–particles (Fig. 4.3), it is to be expected that essentially no first orbit lost α–particle will be stopped by foil layers shallower than 3 μm, nor penetrate deeper than 9 μm. Layers 2 through 3, and 10 were therefore excluded from comparisons against first orbit loss since He in these layers must be due to other sources such as partially thermalized alpha ash or externally introduced He puffs.

In each part of this section, a characteristic of the observed loss is compared to the first orbit loss model, first for the two exposures conducted at a plasma current of 1.0 MA (exposures C & E), then for the two exposures conducted at 1.8 MA (exposures B & D). A comparison is then made with the 90° lost alpha scintillator images for each exposure. Sec. 4.3.1 considers absolute fluence, Sec. 4.3.2 energy distribution, Sec. 4.3.3 pitch angle distribution, and Sec. 4.3.4 radial distribution.

4.3.1 Absolute Fluence

I_p=1.0 MA Absolute Fluence

Fig. 4.5 shows the comparison between the observed fluence (in number of α–particles collected) to the upper and lower rows of outboard facing ports (30°, 75°, 120°) at 1.0 MA (exposures C & E), along with the first orbit loss model predictions generated with the Lorentz ORBIT code (Sec. 4.2.1) for the upper row as a function of collimating port orientation. The first orbit loss model for the lower row is not plotted because it is essentially unchanged from the model for the upper row. The first orbit loss model curve is the predicted alpha collection fraction (as seen in Fig. 4.1 for 1.8 MA exposures) times the total neutron production for each shot. The observed fluence is plotted for the total He content of layers 4 through 9. The observed fluence agrees very well with the first orbit loss model, within the uncertainties discussed in Sec. 4.3.5.

I_p=1.8 MA Absolute Fluence

Fig. 4.6 (analogous to Fig. 4.5) shows the comparison between the observed fluence and the first orbit loss model at 1.8 MA (exposures B & D). The results of the 30° and 75° ports indicate that an anomalously large loss exists, with an alpha fluence roughly an order of magnitude larger than is expected for first orbit loss to the upper rows. This anomalous loss is significantly diminished in the lower rows. The results for the 120° ports, however, appear to be in agreement (keeping in mind that they are near minimum sensitivity) with the first orbit loss model, within the uncertainties discussed in Sec. 4.3.5. This indicates that the anomalous loss does not extend to pitch angles as large as does first orbit loss.

The samples with the largest fluence for each of the 1.8 MA exposures, corresponding to the upper 75° port for exposure B and the upper 67.5° port for exposure D, show increases by factors of 4.7 and 6.4 respectively when the measured fluence in layers 4 through 9 is compared to the predicted fluence for first orbit loss. When

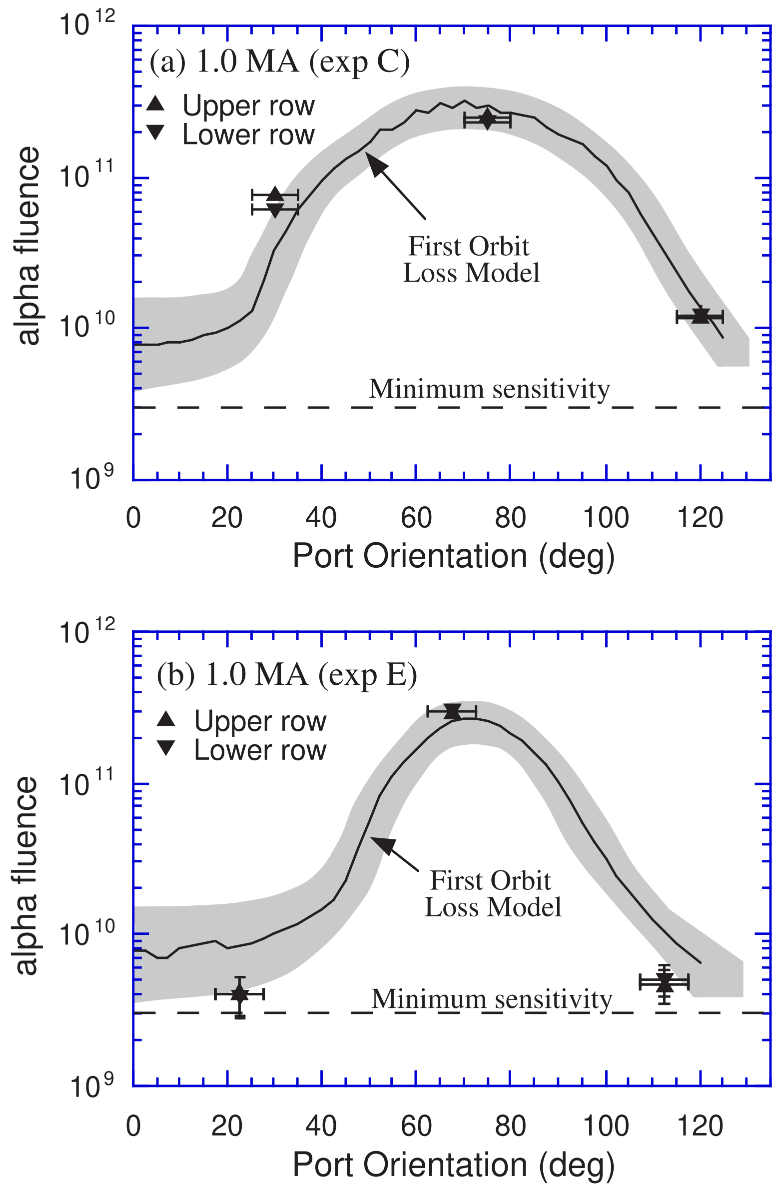

Figure 4.5: *I_p=1.0 MA - Measured fluences of He in layers 4 through 9 for the upper and lower rows of (a) exposure C using the original probe head design, and (b) exposure E using the redesigned probe head, compared with the first orbit loss model calculated with the Lorentz ORBIT code as a function of port orientation. The dashed line, representing the minimum sensitivity, is approximated by multiplying the minimum sensitivity per layer (5×10^8 alphas) by 6 layers. The vertical error for data points above 1.2×10^{10} alphas is $\sim\pm10\%$, corresponding approximately to the height of the triangular data symbol.*

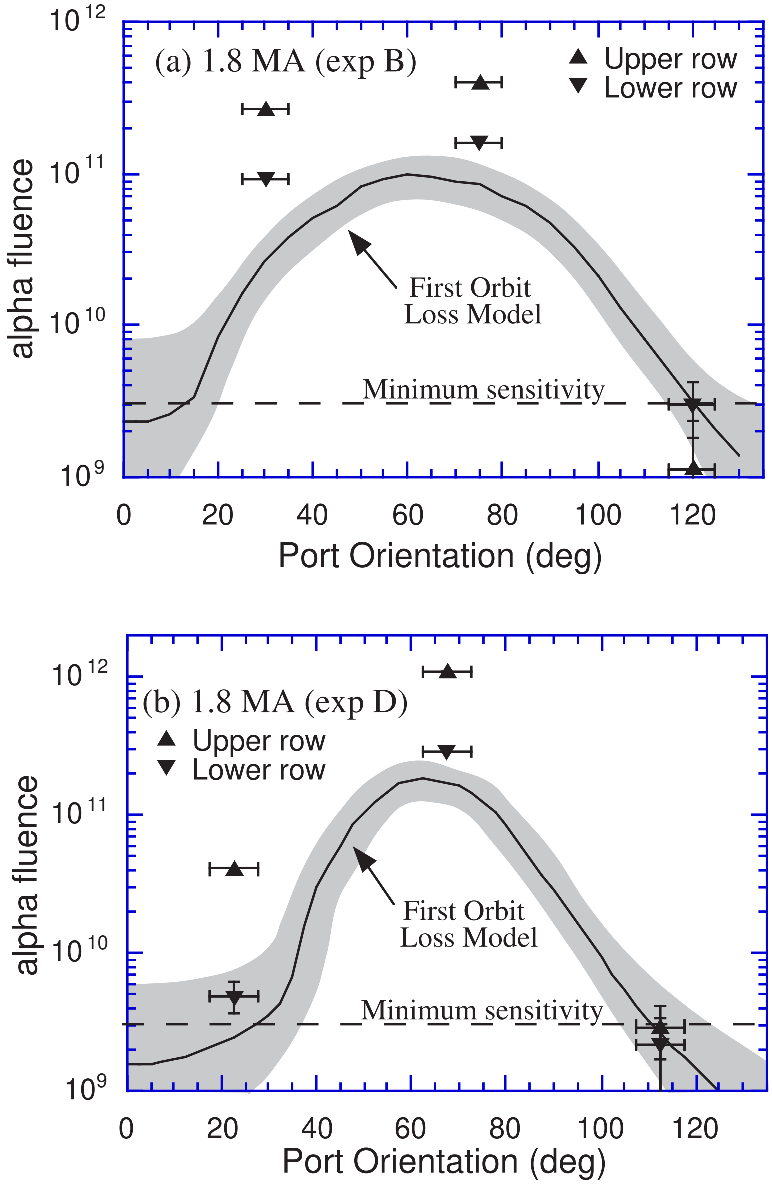

Figure 4.6: *I_p=1.8 MA - Measured fluences of He in layers 4 through 9 for the upper and lower rows of, (a) exposure B using the original probe head design, and (b) exposure D using the redesigned probe head, compared with the first orbit loss model. Same notation as Fig. 4.5. The 30° and 75° ports reveal the existence of an anomalous loss at 1.8 MA.*

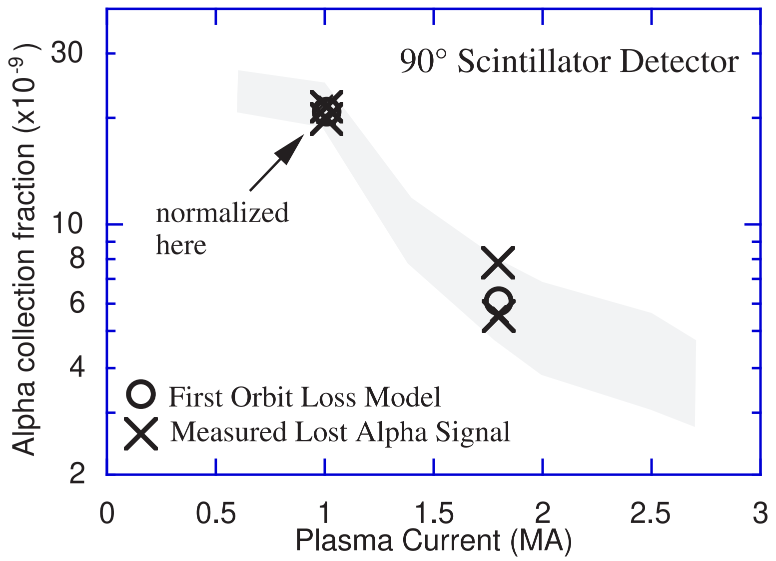

Figure 4.7: *Plasma current dependence of the alpha collection fraction measured with the 90° lost alpha scintillator detector normalized to the first orbit loss model at 1.0 MA. The shaded region corresponds to the first orbit loss model calculated for R=2.52 m plasmas in Ref. [9], but appears to fit the R=2.45 m data well. The good agreement with the model implies that this detector does not 'see' the anomalous loss apparent at 1.8 MA using the alpha collector probe.*

the total measured fluence of layers 2 through 10 is compared to the predicted fluence, both of these samples show an increase by a factor of ∼7. Assuming that the predicted first orbit loss is included in these measurements makes the anomalous loss ∼6 times larger than first orbit loss.

Absolute Fluence to Lost Alpha Detector

Fig. 4.7 shows the dependence of the 90° scintillator signal on plasma current for shots B through E. The data are normalized to the model at 1.0 MA due to uncertainties in the absolute calibration [9]. The gray area overlaid on this plot is taken from the analysis of Ref. [9]. It represents the first orbit loss model with uncertainties as calculated for R=2.52 m plasmas, but appears to fit the model predictions at R=2.45 m quite well. The ratio of alpha loss between 1.0 and 1.8 MA agrees with the first orbit loss model within the uncertainties. There is no increase in the signal at 1.8 MA with respect to the model, consistent with the behavior observed in all other plasma discharges. The first orbit loss model, shown by circles in Fig. 4.7, predicts a drop in the alpha collection fraction by a factor of $\sim$3.4 between 1.0 MA and 1.8 MA. An anomalous loss causing a factor of 7 increase at 1.8 MA, such as that observed by the alpha collector, would make the measured alpha collection fraction, shown by X's in Fig. 4.7, a factor of $\sim$2 larger at 1.8 MA than at 1.0 MA. Hence, it appears that the anomalous loss detected at 1.8 MA with the alpha collector is not seen by the 90° lost alpha scintillator detector.

4.3.2 Energy Distribution

I_p=1.0 MA Energy Distribution

Fig. 4.8 shows the comparison between the measured range distribution and the first orbit loss model of 3.5 MeV α–particles generated with the ORBIT, PORT, and TRIM codes (Sec. 4.2) for the upper and lower row of outboard facing ports at 1.0 MA (exposures C & E). There is reasonable agreement between the observed distribution and the model, with the exception of a low energy loss feature appearing in layers 2 and 3 corresponding to an energy below 2.0 MeV. Although the shape of the peaks lying between layers 4 and 9 do not exactly match the first orbit loss model peaks, the important feature is that the peaks appear in approximately the same layers at an overall magnitude determined in Sec. 4.3.1 to be in agreement with first orbit loss. The disagreement in the specific shape of the distributions may be attributable to the neglect of foil non-uniformities, curvature of the foils, and Doppler broadening of the birth energy distribution (Sec. 4.2). Overall, the agreement is sufficient to conclude that the observations are consistent with the model for first orbit loss with the exception of a low energy loss feature that is not yet understood, but might be related to the anomalous loss at 1.8 MA.

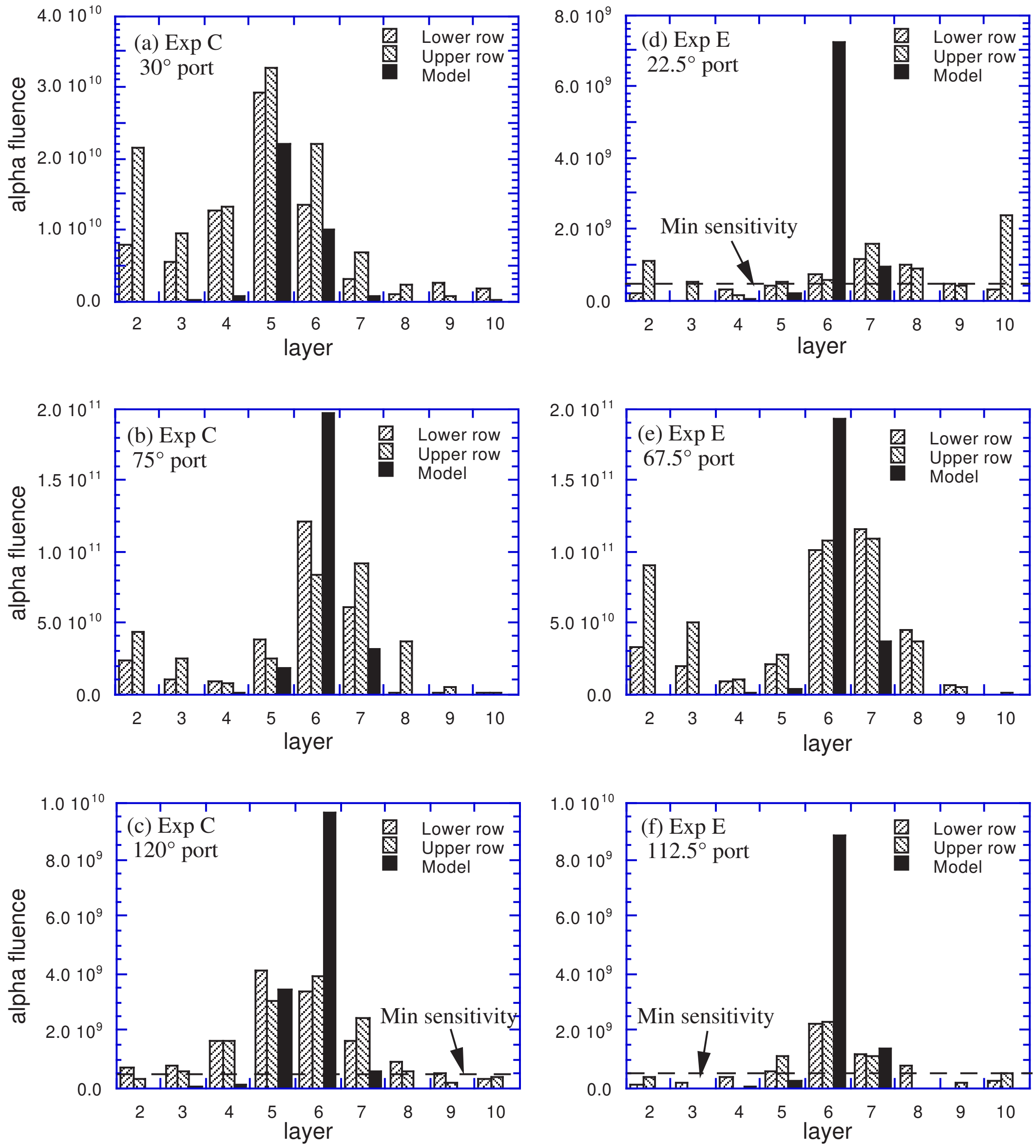

Figure 4.8: *I_p=1.0 MA - Implantation range distributions as a function of layer (i.e. 1 μm bins) for the upper and lower rows and model predictions for (a) 30° (b) 75° and (c) 120° ports of exposure C, and (d) 22.5° (e) 67.5° and (f) 112.5° ports of exposure E. Notice that the vertical scales are linear and not all the same. The plots with a maximum of the vertical scale $\leq 2 \times 10^{10}$ alphas have the minimum sensitivity of the sample analysis ($\sim 5 \times 10^{8}$ alphas/layer) represented by a dashed line.*

I_p=1.8 MA Energy Distribution

Fig. 4.9 (analogous to Fig. 4.8) shows the comparison between the measured range distribution and the first orbit loss model for the upper and lower rows of outboard facing ports at 1.8 MA (exposures B & D). The observed peak in the range distribution occurs at a shallower depth and has a significantly larger width than the first orbit loss model for the 30° and 75° ports of exposure B, and the 67.5° port of exposure D (Figs. 4.9(a, b, e)). This indicates that the anomalous loss occurring at 1.8 MA consists of partially thermalized α–particles.

The data from the 22.5° ports (upper and lower rows) from exposure D (Fig. 4.9(d)) seem to indicate an alpha loss near the birth energy and not the partially thermalized loss mentioned above. This is an indication that the partially thermalized anomalous loss does not occur at pitch angles below the maximum pitch angle accepted by this port ($\sim$49°). Thus, the observed signal should correspond to purely first orbit loss of passing particles. However, as seen in Fig. 4.6(b), the total fluence for layers 4–9 of the upper 22.5° port was nearly 17 times expected first orbit loss. The peak in the sixth layer is repeated in the lower row of the 22.5° port, as seen in Fig. 4.9(d), verifying the lack of a partially thermalized loss to this location. Also, the total fluence for the lower row seen in Fig. 4.6(b) is consistent with first orbit loss. Although there does appear to be an anomalously large signal to the upper row, until this result can be shown to be reproducible, it will be assumed that the loss to this port is purely first orbit loss and is not associated with the partially thermalized anomalous loss observed at 1.8 MA. If this is a valid result, it is associated with a prompt loss mechanism, not the delayed mechanism (allowing for time to slow down) responsible for the partially thermalized anomalous loss.

The peak in the fourth layer of the 75° port of exposure B (Fig. 4.9(b)) corresponds to an alpha loss energy of $\sim$2.2$\pm$0.3 MeV (see Fig. 4.3(a)) if normal incidence is assumed. Similarly, the peak in the fifth layer of the 67.5° port of exposure D (Fig. 4.9(d)) corresponds to an alpha loss energy of $\sim$2.7$\pm$0.3 MeV. Exposure D used the redesigned probe head with the improved collimation (i.e. particles implant closer to normal incidence), and thus provides a better indication of alpha loss energy than does exposure B, which used the original design. It might also be inferred from the

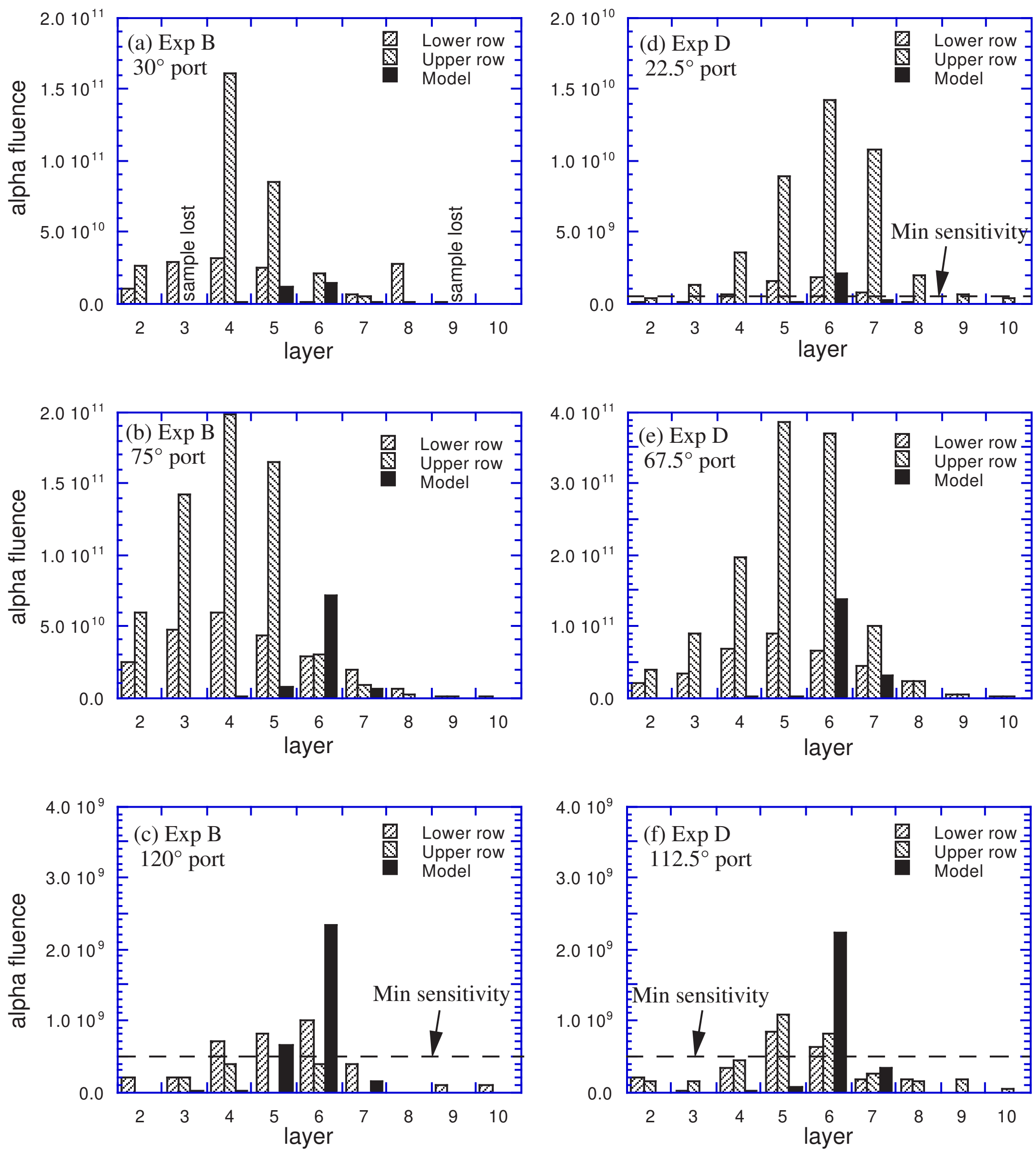

Figure 4.9: *I_p=1.8 MA - Implantation range distributions as a function of layer for the upper and lower rows and model predictions for (a) 30° (b) 75° and (c) 120° ports of exposure B, and (d) 22.5° (e) 67.5° and (f) 112.5° ports of exposure D. Same notation as Fig. 4.8. Layers 3 and 9 of the upper row of the 30° port of exposure B in (a) were lost during the tritium decontamination process [31].*

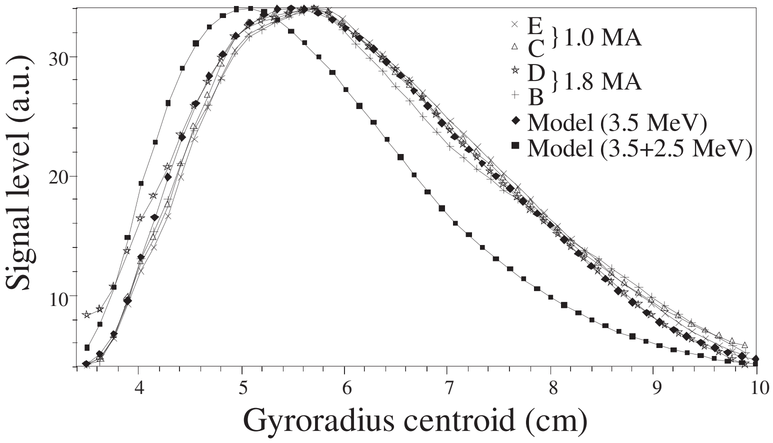

Figure 4.10: *Gyroradius distributions of alpha loss as measured with the 90° lost alpha scintillator detector averaged over toroidal pitch angle, from 45° to 90°, and time, from 3.4 to 3.7 sec (i.e. the quasi-steady state portion of the discharge). Model curves are plotted for 3.5 MeV α–particles and equal fluxes of 2.5 MeV and 3.5 MeV α–particles after being corrected for the finite aperture sizes and optical resolutions of the detectors. The curves are normalized vertically to each other near their peaks, but the horizontal axes were absolutely calibrated by an in-vessel alignment to within $\sim$1 cm.*

deeper implantation range in exposure D that the 7.5° clockwise rotation that went into the redesign was such as to bring the axis of the port closer to the pitch angle of the anomalous loss, also allowing particles to implant closer to normal incidence. In other words, the anomalous loss probably occurs at a pitch angle closer to 67.5° than to 75°. Assuming the two 1.8 MA exposures are exposed to an anomalous loss of the same energy, the peak of the energy distribution is inferred to be $\sim$2.5 $\pm$ 0.3 MeV (i.e. $\sim$70$\pm$10% of the birth energy). In the discussion of Sec. 4.4, the anomalous loss at 1.8 MA will be simplified as having a single loss energy of 2.5 MeV.

Energy Distribution to Lost Alpha Detector

The gyroradius distributions for exposures B through E as measured with the 90° lost alpha scintillator detector are shown in Fig. 4.10. Two model curves, taking into account the finite aperture sizes and optical resolutions of the detectors, are also plotted. The distributions show good shot to shot consistency, independent of the plasma current, and they agree closely with the model assuming alpha loss at a single energy of 3.5 MeV. For comparison with what might be expected if some of the anomalous loss observed with the alpha collector were also detected by the 90° scintillator detector, the other model assumes equal loss components at energies of 2.5 MeV and 3.5 MeV. These distributions provide further evidence that the lost alpha scintillator detectors do not detect the partially thermalized anomalous loss observed with the alpha collector at 1.8 MA, which was inferred to be up to 6 times the first orbit loss at an energy of ~2.5 MeV.

4.3.3 Pitch Angle Distribution

I_p=1.0 MA Pitch Angle Distribution

The first orbit model predictions in Figs. 4.5 and 4.6 are just the expected pitch angle distributions corrected for the geometric resolution of the detector (Sec. 4.2). So the pitch angle distributions of Fig. 4.5 for the exposures at a plasma current of 1.0 MA (C & E) show good agreement between the observations and the first orbit loss model. However, the wide pitch angle acceptance of the collimating ports (±45° for the original design; ±27° for the redesign) result in relatively poor pitch angle resolution. To obtain improved information pertaining to the pitch angle distribution, it was decided to cut selected samples vertically in half to compare the fluences contained in the right and left halves. A loss at a pitch angle larger than the collimating port's orientation tends to concentrate He in the left half of the foil stack, assuming $\rho \gg w, d$ and $\chi_0 > 0$ (see Secs. 3.3 and 4.2.2 for symbol definitions).

The PORT code was used to predict the fraction of alpha fluence implanted in the left half of the foil stack, referred to as the left collection fraction, for the pitch angle distribution generated for first orbit loss using the Lorentz ORBIT code. In other words, the left collection fraction L is:

$$L = \frac{l}{l + r} \tag{4.2}$$

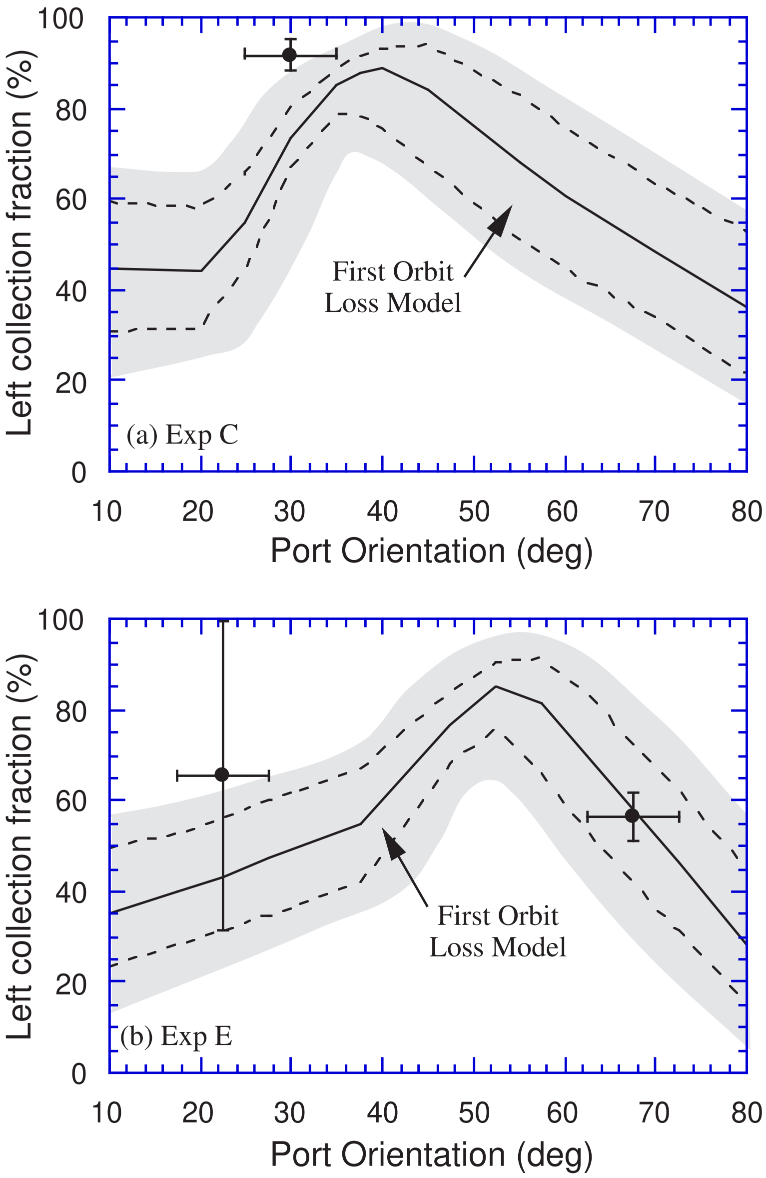

Figure 4.11: *I_p=1.0 MA - Left collection fraction as a function of port orientation for the upper row of the (a) 30° port of exposure C, and (b) 22.5° and 67.5° ports of exposure E. The left collection fraction is the fraction of He in layers 4 through 9 that implanted in the left half of the stack. The model is based on the first orbit loss pitch angle distributions calculated using ORBIT. The dashed lines represent the model assuming the cut is made 10% of the port width to the right (upper dashed line) or left (lower dashed line) of center.*

where l and r are the amounts of He contained in the left and right halves respectively. Fig. 4.11 shows a comparison between the fraction of He detected in the left half for the selected samples at 1.0 MA and the model prediction as a function of port orientation. The solid line represents the expected left collection fraction assuming the cut was made right down the middle of the foils. The dashed lines represent the expected left collection fractions for the cases where the cut is made just 10% to the left or right of center of the port diameter (i.e. ~0.6mm). Notice that the model appears to slightly underestimate the left collection fraction at the 30° port. A possible explanation for this will be discussed in Sec. 4.3.5. Otherwise, there is reasonable agreement between the first orbit loss model and the data.

I_p=1.8 MA Pitch Angle Distribution

Fig. 4.12(a) (analogous to Fig. 4.11) shows the comparison between the fraction of He detected in the left half of the foil stacks for the 22.5° and 67.5° ports of exposure D and the model prediction as a function of port orientation. Again, notice that the model appears to underestimate the left collection fraction at the 22.5° port. The observation at 67.5° is in good agreement with the model for 3.5 MeV α–particles lost with the pitch angle distribution calculated using the Lorentz ORBIT code. However, the majority of the loss detected by this port is the partially thermalized anomalous loss.

The PORT code was used to find the toroidal pitch angle for the anomalous loss that produces the best match to the observed left collection fraction. This assumes that the anomalous loss can be represented by a loss at a single pitch angle and single energy of 2.5 MeV. Fig. 4.12(b) shows that the measured left collection fraction, at ~36%±5%, best matches the model for 2.5 MeV α–particles at a toroidal pitch angle of ~63°±7°. The toroidal pitch angle of the fattest banana orbit χ_{fb} which corresponds to the boundary between passing and trapped particles was seen in Fig. 3.7 to occur at $\chi_{fb} \approx 56°$ for $I_p = 1.8$ MA. Thus it is concluded that $\chi_{anom} > \chi_{fb}$ under the preceding assumptions.

The extent of the anomalous loss in pitch angle can be further narrowed down by

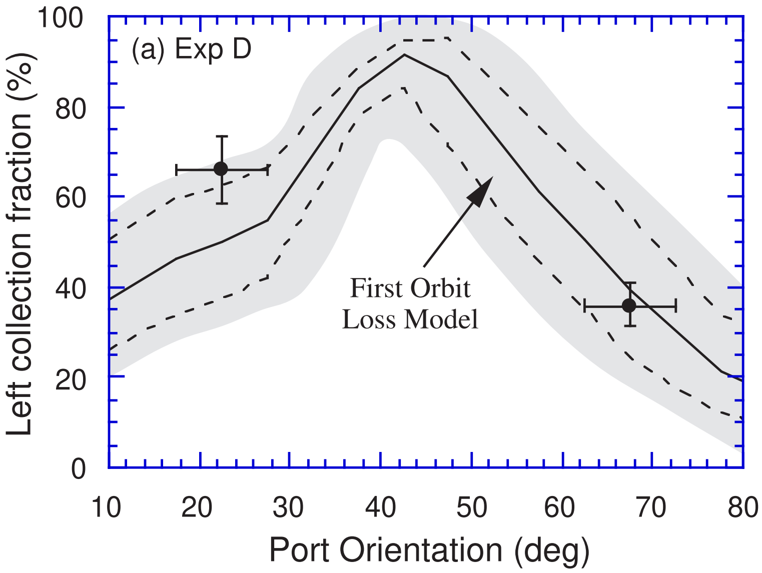

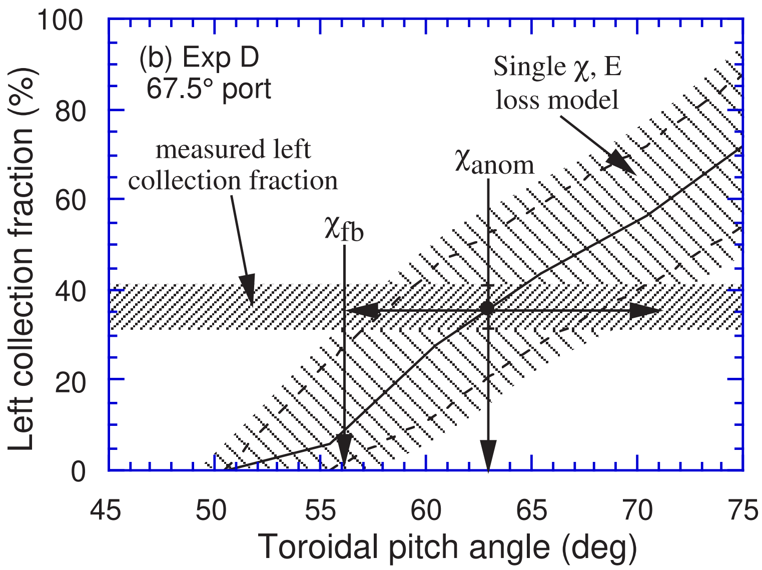

Figure 4.12: *I_p=1.8 MA - (a) Left collection fraction as a function of port orientation for the upper row of the 22.5° and 67.5° ports of exposure D, analogous to Fig. 4.11. (b) Left collection fraction for the upper 67.5° port of exposure D fit to a model based on alpha loss at a single energy (2.5 MeV) and a single toroidal pitch angle as a function of this pitch angle. From the data, a toroidal pitch angle for the anomalous loss of 63°±7° is inferred.*

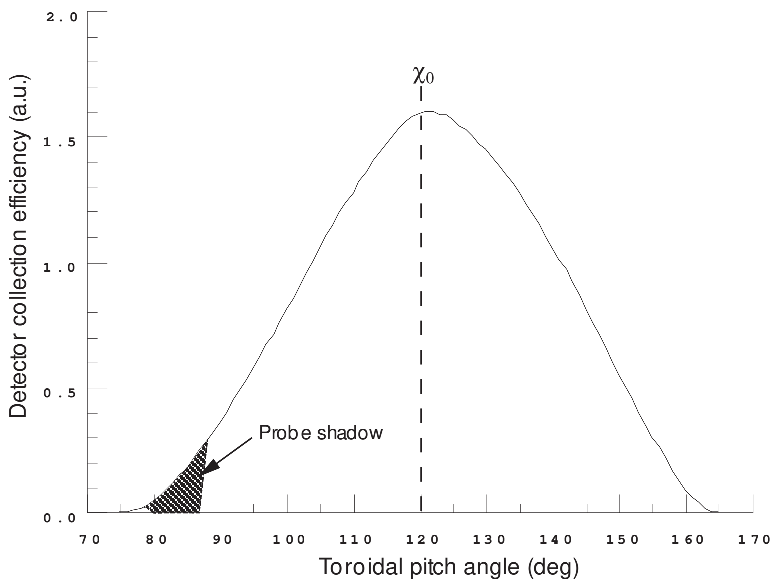

Figure 4.13: *I_p=1.8 MA - Relative detector collection efficiency as a function of toroidal pitch angle for the 120° port of the original probe head design (exposure B). The collection efficiency drops off away from the pitch angle of the port axis (χ_0) due to collimation, and is cut off at ±45° either side of χ_0. The probe shadow occurs near a true pitch angle of $\chi = 90°$ ($\chi_t = \chi - \chi_{bt} \approx 85°$) where the gyro-orbit of a high energy ion intercepts the probe head.*

its absence in some of the detector samples. The pitch angle distributions of Fig. 4.6 for the exposures at a plasma current of 1.8 MA (B & D) show that there is no anomalous loss being detected by the 120° (112.5°) port of exposure B (D), indicating that the anomalous loss does not extend to pitch angles as large as first orbit loss as previously mentioned in Sec. 4.3.1. Fig. 4.13 shows the relative detector collection efficiency (i.e. the fraction of particles that reach the foil without being stopped by collimation), assuming flat pitch and gyro angle distributions, as a function of the toroidal pitch angle, $\chi_t = \chi - \chi_{bt}$ (Sec. 4.2.2), for the 120° port of exposure B for α–particles at 2.5 MeV (the representative anomalous loss energy). The pitch angle acceptance of ±45° for the original probe design, centered approximately about the port's orientation of 120° for exposure B can be seen in this figure. Incidentally, the data from this port represents the first experimental measurement of particles escaping to the TFTR wall on counter-going orbits (i.e. $\chi > 90°$). Although the signals are small in the 120° ports, as evidenced in Figs. 4.5 through 4.9, the results appear to be consistent with first orbit loss.

Also shown in 4.13 is the self-shadowing effect of the probe head. This shadowing is the result of insufficient displacement of an α–particle along the magnetic field line making the α–particle unable to clear the probe head in one gyro-orbit when the true pitch angle, χ, is near 90° ($\chi_{bt} = 4.6°$ for a 1.8 MA exposure explains the shift away from $\chi_t = 90°$ in Fig. 4.13). So, with the exception of a small degree of acceptance at 75° to 80° for exposure B, the effective minimum toroidal pitch angle cutoff occurs at $\chi_t > 87°$. The use of the redesigned probe, with its smaller pitch angle acceptance range in exposure D, is slightly more restrictive. This sets the upper limit on the toroidal pitch angle of the anomalous loss at 87°.

Similarly, the toroidal pitch angle acceptance for the 30° (22.5°) port extends up to $\chi_t = 75°$ (49.1°) for exposure B (D). Probe shadowing is not a factor in these ports since pitch angles near 90° are excluded. It was seen in Sec. 4.3.2 that the partially thermalized anomalous loss was detected in the 30° port of exposure B, but not in the 22.5° port of exposure D (although the anomalously large alpha fluence in this port is not fully understood). Thus the anomalous loss occurs at toroidal pitch angles $\chi_t < 75°$, but not at $\chi_t < 49°$. This sets the lower limit on the toroidal pitch angle of the anomalous loss, χ_{anom}, at 49°. Combining these results yields, $49° \leq \chi_{anom} \leq 87°$. It might, however, be expected that a feasible anomalous loss mechanism would preferentially provide either trapped or passing particles. Since the best fit in Fig. 4.12(b) gave $\chi_{anom} > \chi_{fb}$, trapped particles are probably the main constituent of the anomalous loss. It thus seems likely that the anomalous loss pitch angle distribution is concentrated in a narrow range above the passing-trapped boundary (i.e. $56° < \chi_{anom} < 87°$).

Pitch Angle Distribution to Lost Alpha Detector

The toroidal pitch angle distributions measured with the 90° lost alpha scintillator detector are shown in Fig. 4.14. For comparison, the Lorentz ORBIT generated pitch angle distributions are plotted after being corrected for the geometric and optical resolutions of the detectors. Notice that the model at I_p=1.0 MA in Fig. 4.14(a)

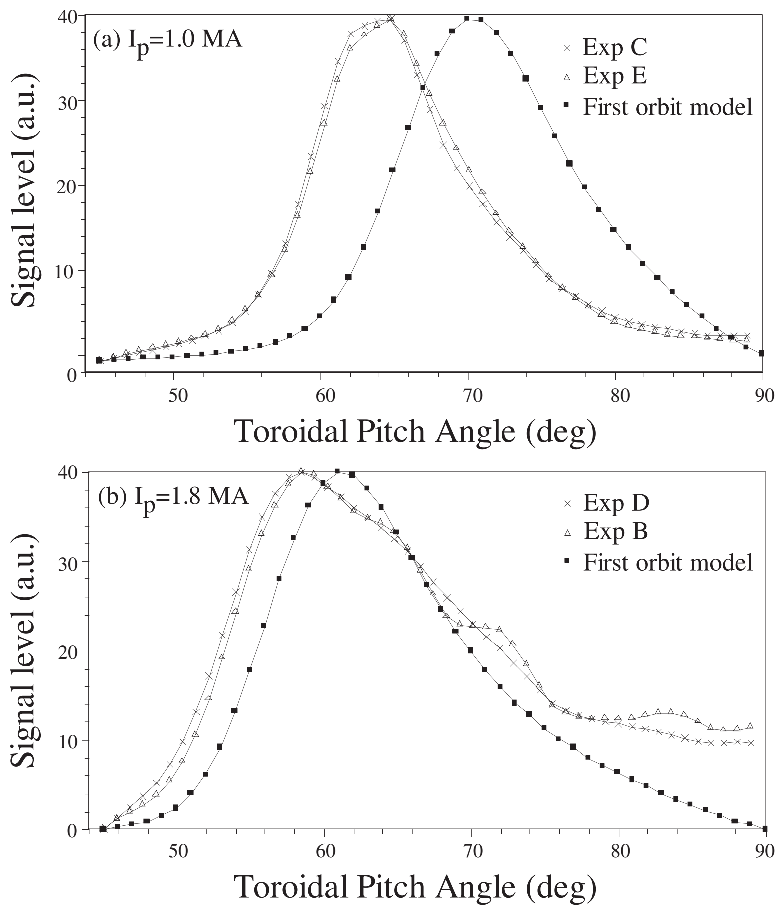

Figure 4.14: *Toroidal pitch angle distributions of alpha loss as measured with the 90° lost alpha scintillator detector averaged over gyroradius, from 3.5 to 9.9 cm, and time, from 3.4 to 3.7 s. Model curves are plotted for the ORBIT calculated first orbit loss after being corrected for the finite aperture sizes and optical resolutions of the detectors. The curves are normalized vertically to each other near their peaks, but the horizontal axes were absolutely calibrated by an in-vessel alignment to within ∼3°.*

tends to overestimate the toroidal pitch angle of first orbit loss (i.e. the model is shifted to the right of the measured distribution) by $\sim 6°$. This discrepancy will be referred to in Sec. 4.3.5. The peaks of the I_p=1.8 MA distributions in Fig. 4.14(b), however, agree to within the 3° uncertainty associated with the scintillator detectors. The shapes of the model distributions are in reasonable agreement with the measured ones. The distribution at 1.8 MA appears to be somewhat wider than predicted, but there is no indication of an anomalously large loss occurring at a pitch angle above the fattest banana orbit.

4.3.4 Radial Distribution

I_p=1.0 MA Radial Distribution

It is apparent from Fig. 4.5 that the fluences of α–particles at a plasma current of 1.0 MA to the upper and lower rows of outboard ports are comparable. Fig. 4.15 shows the fluence levels for the 1.0 MA exposures (C & E) measured in layers 4–9 (representing first orbit loss) of the 75° upper and lower ports and compares them to the first orbit loss model as a function of detector height as measured from the midplane. The modeled fluence drops sharply about 1.0 cm outside the RF limiter radius due to the shadowing effect of the limiter. The shadow occurs outside of the RF limiter radius as a result of the combination of the outward bulge of the magnetic field (by $\sim$1.5 mm [38]) between TF coils associated with TF ripple, and the downward drifts (∇B and curvature) that an α–particle experiences during its transit from the limiter to the probe. So, although the lower row of ports was placed below the RF limiter, these effects are sufficient to keep the lower ports out of the limiter shadow for first orbit loss.

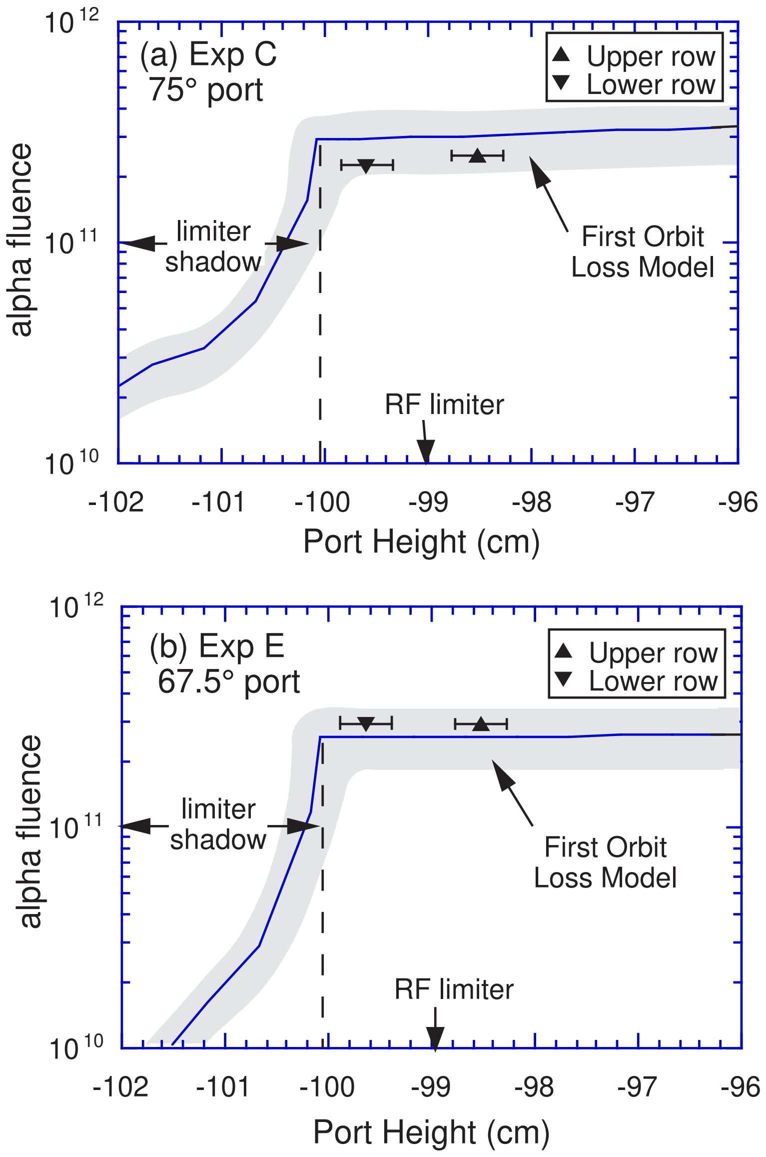

Figure 4.15: *I_p=1.0 MA - Alpha fluence for layers 4 through 9 as a function of port height for the upper and lower rows of the (a) 75° port of exposure C, and (b) 67.5° port of exposure E. The RF limiter shadow begins ∼4 mm below the midplane of the lower row.*

I_p=1.8 MA Radial Distribution

Fig. 4.6 showed that the fluences of α–particles at a plasma current of 1.8 MA for the 30° and 75° ports drop by a factor of 3 or more between the upper and lower rows. Fig. 4.16 (analogous to Fig. 4.15) shows the fluence levels for the 1.8 MA exposures (B & D) of the 75° upper and lower ports and compares them to the first orbit loss model as a function of detector height. A strong radial dependence is clearly present among the 1.8 MA anomalous loss data. It is unclear whether this radial dependence is due to the RF limiter shadowing or a radial diffusive loss of α–particles. The shadowing effect of the limiter increases when the α–particle orbits stay closer to the magnetic field lines, as occurs with decreased α–particle energy, decreased α–particle pitch angle, or increased plasma current. Lorentz ORBIT code simulations show that for a 2.5 MeV α–particle, the limiter shadow is brought only $\sim$1 mm closer to the RF limiter radius than is shown in Fig. 4.16 for first orbit loss, making it unlikely that the strong radial dependence is due solely to limiter shadowing. A diffusive loss having a finite random radial step-size between toroidal transits, could give rise to a radial dependence near absorbing boundaries such as the RF limiter and the probe head itself (Sec. 4.4.3). Further experiments that vary the radial position of the probe would be necessary to obtain a conclusive result. However, the strong radial dependence is further evidence that the 1.8 MA loss is not pure first orbit loss.

Radial Distribution to Lost Alpha Detector

The 90° scintillator detector with which the alpha collector results are compared is fixed in position such that a radial scan is not possible. As pointed out in Sec. 2.5.1, the pinhole aperture of the scintillator detector is located $\sim$0.9 cm lower than the top of the lower row of the alpha collector. Therefore, the strong radial dependence of the anomalous loss might explain why it isn't observed on the 90° scintillator.

The scintillator detector located 20° below the outer midplane is, however, movable. Radial scans have been accomplished using this probe to investigate the diffusive nature of stochastic ripple diffusion (SRD) of fusion products. SRD (Sec. 2.3.2) causes

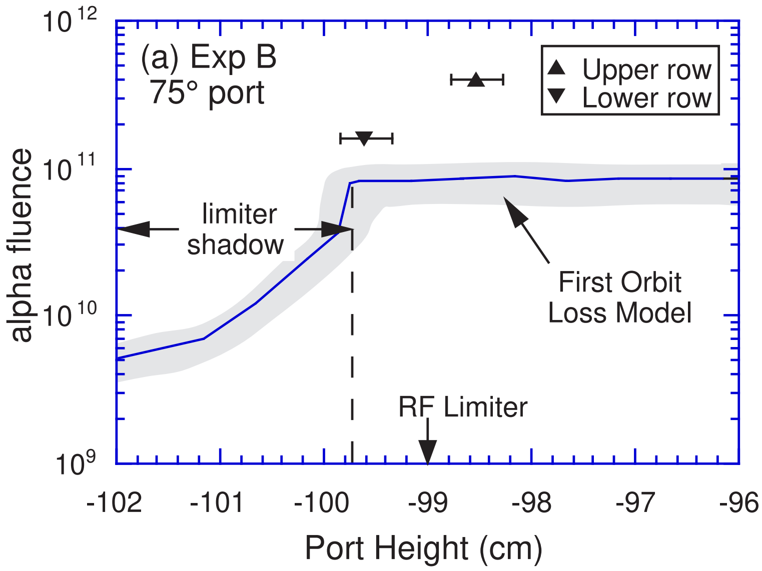

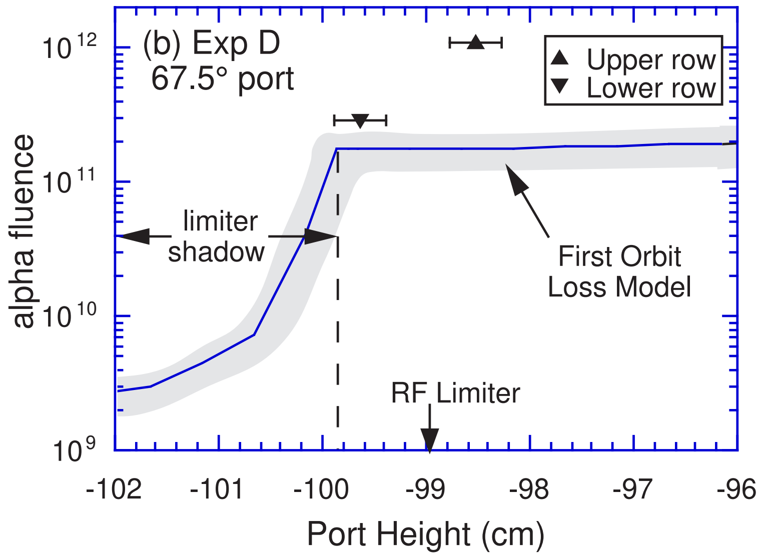

Figure 4.16: *I_p=1.8 MA - Alpha fluence for layers 4 through 9 as a function of port height for the upper and lower rows of the (a) 75° port of exposure B, and (b) 67.5° port of exposure D. The RF limiter shadow begins only ∼2 mm below the midplane of the lower row, possibly placing the lower row partially in the shadow. The decrease in the anomalous loss from the upper to lower row may be attributable to shadowing and/or a radial diffusive loss.*

α–particles to be lost near their birth energy and can be the dominant loss mechanism in a narrow poloidal region about the outer midplane. These scans have shown a radial dependence of alpha loss comparable to that of the 1.8 MA anomalous loss observed using the alpha collector (i.e. $\sim$ a factor of 3 decrease for $\sim$1 cm radially outward movement near the RF limiter edge). There have not, however, been any indications of a partially thermalized loss to the 20° scintillator detector.

4.3.5 Uncertainties

The minimum experimental uncertainty in the alpha fluence measurement is estimated to be equal to the minimum detectable fluence of $\sim \pm 5 \times 10^8$ alphas per sample [32]. For Figs. 4.5, 4.6, 4.15, and 4.16, where the fluence of layers 4 through 9 (6 layers) are summed, the minimum uncertainty is $\sim 1.2 \times 10^9 (\approx \sqrt{6} \times 5 \times 10^8)$. For summed fluences $\geq 1.2 \times 10^{10}$ alphas, the experimental uncertainty is estimated to be $< \pm 10\%$ [32], corresponding approximately to the height of a data point (i.e. triangle symbol) on this semilog scale.

The 5° uncertainty in the port orientation assigned to the data points in Figs. 4.5, 4.6, 4.11, and 4.12(a), corresponds to $\sim$2 mm on the circumference of the probe. This is the maximum misalignment that might be expected from the method used to align the probe head onto its base, combined with the uncertainty in the base alignment with respect to the vessel. The uncertainty in the port height assigned to the data points in Figs. 4.15 and 4.16 is 0.25 cm.

The error in the first orbit loss model represented by the shaded region in Figs. 4.5, 4.6, 4.15, and 4.16, is based on several uncertainties. First of all, the source and current profiles used by the Lorentz ORBIT code are taken from TRANSP for one time during the flat top portion in the discharge. These profiles are used to represent the plasma for the entire duration of the shot. Performing the calculation for other times throughout the discharge results in less then 15% variation in the total fluence calculation. So the choice of a single time near the time of maximum fusion rate should introduce no more than 15% error. Another error in the first orbit loss model comes from converting the alpha collection fraction in α–particles per neutron to total loss fluence by multiplying by the global neutron production. The global neutron measurements have an $\sim$7% error associated with them [39], which is transferred to the alpha fluence calculation. Combining these uncertainties, along with other sources of uncertainty such as the accuracy of the TRANSP profiles, the overall minimum error in the first orbit loss model is estimated to be $\pm$30%. This uncertainty is based on the modeling of the 75° port. The 22.5° port can have substantially more error since the main contribution of α–particles to this port is from co-going α–particles born near the edge of the plasma (e.g. the 40° orbit of Fig. 3.7), and is thus extremely sensitive to uncertainties in the source profile which can greatly affect the source term at the edge. The 75° port fluences are dominated by α–particles lost near the fattest banana orbit which pass closest to the magnetic axis where the source profile is peaked and are thus not as sensitive to the shape of the profile. The uncertainty due to the source profile was estimated using the results of a sensitivity analysis in which a parabolic to a power source profile was assumed: $S(r) = S_0(1-(r/a)^2)^{i_s}$, where $S(r)$ is the source profile as a function of minor radius r, S_0 is the alpha source term at the magnetic axis, a is the edge minor radius, and i_s is the source term peaking exponent. The Lorentz ORBIT calculated alpha collection fraction was evaluated for $i_s = 8 \pm 1$, a common value for the peaking exponent with a reasonable uncertainty. Where the alpha collection fraction varied by more than $\pm$30%, the higher uncertainty due to source profile sensitivity was used.

The first orbit model also incorporates a $\pm 5°$ uncertainty in the port orientation which comes about due to uncertainties in the plasma current profile and modeling inaccuracies of the vacuum magnetic field in the Lorentz ORBIT code. As illustrated in Fig. 4.14, the first orbit model does not match the pitch angle distribution measured by the scintillator in the 1.0 MA case. Correcting this overestimate would roughly correspond to a shift of the model distributions to the left by $\sim 5°$. The agreement between the data and the model for the 1.0 MA distributions, shown in Figs. 4.5 and 4.11, would be improved by such a shift. To account for this uncertainty, the first orbit model is given a $\pm 5°$ spread.

The uncertainty in the left collection fraction data of Figs. 4.11 and 4.12 is based on comparing the maximum and minimum possible measured alpha fluences, using a measurement uncertainty of the larger of $\pm 1.2 \times 10^9$ α–particles or $\pm 10\%$, for the left and right halves.

4.4 Discussion

4.4.1 Summary of Experimental Results

Measurements of escaping α–particles were made using the alpha collector probe for plasma currents of 1.0 and 1.8 MA. The He released from foil layers 4 through 9, which should be representative of first orbit lost α–particles, was then compared to a first orbit loss model with respect to the total alpha fluence implanted into these foils, and the energy, pitch angle and radial distributions inferred from the measured loss. The comparison at 1.0 MA indicates that the measurement from layers 4 through 9 is consistent with the first orbit loss model for 3.5 MeV α–particles. The shallow layers (2 through 3), however, suggest that a small ($\sim$1/3 the fluence of first orbit loss), low energy ($<$ 2.0MeV) anomalous loss feature may be occurring at this plasma current.

The comparison at 1.8 MA reveals a partially thermalized loss with a total alpha fluence nearly an order of magnitude ($\approx 7\times$) larger than that of the first orbit loss model and a wide energy distribution peaked at $\sim$2.5$\pm$0.3 MeV(i.e. $\sim$30% below the birth energy of 3.5 MeV). The pitch angle distribution of the inferred anomalous loss appears to occur in a narrow region above the passing-trapped boundary ($\chi_{fb} \approx 56°$) and is peaked at a toroidal pitch angle of $\sim 63° \pm 7°$. This anomalous loss drops by approximately a factor of 3 in magnitude from the upper row to the lower row of collimating ports (separated by $\sim$1.1 cm), in contrast to the first orbit loss model which remains nearly constant between the two rows. There is no evidence of this anomalous loss on the 90° lost alpha scintillator detector.

4.4.2 Comparison of 1.8 MA Anomalous Loss with Delayed Loss

The anomalous results obtained with the alpha collector probe are qualitatively similar to an anomalous loss feature called 'delayed loss', which is not yet understood [40]. Delayed loss is observed with the 90° lost alpha scintillator detector for DD fusion products (i.e. 3 MeV proton, and 1 MeV triton) in DD plasmas. Delayed loss, however, has not been observed with the scintillator detectors for DT α–particles [9]. The following is a list of the observed characteristics of delayed loss and how they compare to the anomalous loss observed with the alpha collector probe.

1. Delayed loss is seen at the scintillator detector located 90° poloidally below the outer midplane (i.e. at the bottom of the TFTR vessel), but not at the 20°, 45° nor 60° detectors. This is consistent with the current results in that the measurements made with the alpha collector probe were only made at the bottom of the vessel.

2. The delayed loss to the 90° scintillator detector has a strong dependence on the plasma major radius, being largest at the small major radius of R=2.45 m, and disappearing at $R > 2.55$m. Again, this is consistent with the current results in that the measurements made with the alpha collector probe were made in R=2.45 m plasmas. The alpha collector was used only in these small plasmas to minimize probe heating by maximizing its distance from the plasma. The design does allow its use in up to R=2.52 m plasmas, but no exposures were done at this radius.

3. The strength of delayed loss increases with respect to the first orbit loss with increased plasma current, becoming dominant above 1.8 MA. This is consistent with the result that only first orbit loss (with the exception of a small anomalous loss feature at low energy) was observed at 1.0 MA, but a large anomalous loss, in addition to first orbit loss, was observed at 1.8 MA using the alpha collector probe. The total loss (first orbit plus delayed loss) in DD at 1.8 MA as measured with the 90° scintillator detector was about a factor of 2 above the expected

first orbit loss [40], as compared to a factor of 7 for the alpha collector in DT at 1.8 MA.

4. The energy of delayed loss particles is about half (i.e. 55±15% [40]) that of the prompt first orbit loss, as inferred from the gyroradius of its scintillator impact. This is consistent, within the energy resolution of the detectors, with the ∼70±10% of birth energy inferred for the anomalous loss of the alpha collector.

5. Delayed loss at I_p=1.8 MA occurs at a pitch angle approximately 10° above that of the fattest banana orbit. This is roughly consistent with the anomalous loss pitch angle inferred to be ∼7°±7° above the fattest banana pitch angle of 56°.

6. Delayed loss is delayed by ∼200±100 ms with respect to the usual first orbit loss, as can be seen most clearly at the beginning and end of neutral beam injection. The time resolution of the alpha collector is limited to a single discharge since it integrates α–particles over an entire shot. Thus this feature of delayed loss can not be checked with the alpha collector. However, the inferred energy of ∼70±10% of the birth energy for the anomalous loss requires a delay of ∼100 ms for them to slow down to this energy (assuming an energy e-folding time of ∼200 ms) consistent with delayed loss.

7. Delayed loss increases slowly with NBI power at a fixed plasma current. The alpha collector exposures were all done at an NBI power of ∼10 MW. Thus a comparison of the NBI power dependence of the two anomalous losses can not be made. The design of the collector probe does allow its use in full power discharges, making a beam power scan possible, but such a scan was not done.

8. For R=2.45m and I_p=1.8 MA plasmas, delayed loss to the 90° scintillator detector is of the same order of magnitude as first orbit loss in DD plasmas, but is absent in DT plasmas. The anomalous loss to the alpha collector appears to be about a factor of 6 times larger than first orbit loss in DT plasmas. The alpha collector is not capable of detecting DD fusion products. The lack of detectable levels of delayed loss on the scintillator detector in DT plasmas but apparently large levels in the alpha collector is most likely due to the different radial positions of the two probes. The lower row of the alpha collector extends

nearly 1 cm farther into the vessel than does the pinhole aperture of the 90° scintillator detector (Sec. 3.5). The strong radial dependence of the anomalous loss, seen in the upper/lower row comparisons of Fig. 4.16, may be sufficient to make it an insignificant contribution to the loss observed by the scintillator detector. Their different toroidal positions relative to toroidal asymmetries in the vessel such as limiters and the path of neutral heating beams may also be a factor.

It may be significant to note that the delayed loss features changed significantly when the 90° scintillator detector was repositioned after the 1990 run to accommodate the installation of a new poloidal RF limiter [40]. Previously, the detector aperture was located about 4 cm radially outside (i.e. below) and about 120° toroidally from the edge of the nearest limiter. The new limiter was installed only 45° toroidally from this detector which forced a relocation of its aperture to only about 1 cm below the edge of this new limiter to avoid shadowing of the aperture [41]. After the repositioning, the delayed loss feature increased in magnitude (by a factor of $\sim$4 at I_p=1.8 MA) and peaked at a pitch angle closer to the passing-trapped boundary. The implication was that after its repositioning, the 90° detector collected more anomalous delayed loss at low pitch angles than it had previously, presumably because these ions had not reached the aperture of the detector in the 1990 run. The first orbit loss features remained essentially unchanged between the two runs. This demonstrates the fact that delayed loss is extremely sensitive to the relative positioning of a detector at 90° and the obstacles that fusion products may encounter such as RF limiters.

The similarities between delayed loss and the anomalous loss observed with the alpha collector imply that they may be due to the same loss mechanism. In Sec. 4.5 some of the possible loss mechanisms are considered.

4.4.3 Trajectories of anomalous loss orbits

The trajectory of an α–particle's last orbit prior to intersection with the detector can be calculated using the Lorentz ORBIT code. Fig. 4.17 shows the last orbit traced

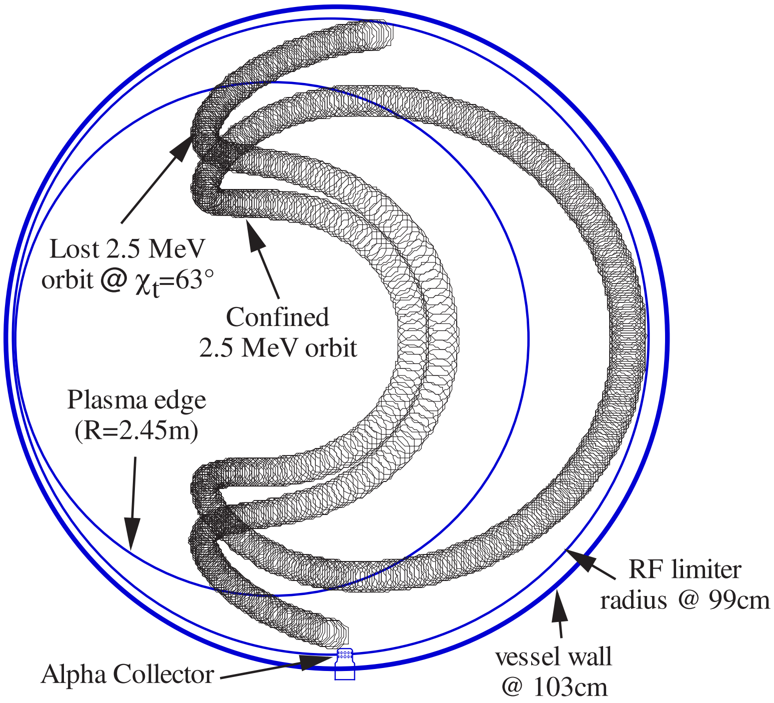

Figure 4.17: *Trajectories in a R=2.45 m, I_p=1.8 MA plasma of an anomalous loss orbit (2.5 MeV, χ_t=63°) that strikes the detector at the bottom of the TFTR vessel and a marginally confined orbit with the same parameters that just misses the RF limiter at the outer midplane. The banana tips of the two orbits are displaced by ∼17 cm.*

backwards in time from the alpha collector at the bottom of the vessel to an RF limiter at the top of the vessel for an α–particle at E =2.5 MeV and χ_t=63° (the parameters inferred for the anomalous loss) for the R=2.45m, I_p=1.8 MA discharge of exposure B. Also shown in Fig. 4.17 is a marginally confined orbit of the same energy which was started with an upward vertical displacement of the lower banana tip of ∼17 cm with respect to the last orbit. The outer leg of this confined orbit just barely misses the projection of the RF limiter (centered at R=2.61m with a minor radius of 0.99 m) near the outer midplane. Thus, confined orbits with banana tips just below this one intersect the wall just below the outer midplane. Therefore, the anomalous loss orbits detected at 90° could be brought there by a relatively large vertical step on the last bounce of a previously confined trapped orbit, while smaller vertical steps would cause the loss to occur nearer the outer midplane, as is the case for stochastic ripple diffusion [10].

A detailed study of many such anomalous loss orbits such as those in Fig. 4.17 has shown that the vertical displacement of the lower banana tip required for a previously confined orbit to reach the alpha collector at the bottom of the vessel (for $E = 2.2$ to 2.8 MeV alpha orbits within $\chi_t = 56° - 70°$) is at least 15 cm. Such a large step-size, however, is inconsistent with the observed radial dependence of the anomalous loss. The 1.1 cm separation between the upper and lower rows of ports is much less than the required step-size of >15 cm. Thus there should be little variation in the alpha fluence between the rows, but measurements show a factor of 3 difference between the upper and lower row.

If α–particle orbits could scrape off at the bottom of the vessel (rather than at the outer midplane) as they diffuse outwards, then small step-size radial diffusion could explain the observed radial dependence and absence of the anomalous loss on the scintillator detectors. However, as can be inferred from Fig. 4.17, the probe would have to be placed ~20 cm further into the vessel to intercept a marginally confined α–particle orbit with the anomalous loss parameters. A smaller banana width could allow an α–particle orbit to strike the bottom of the vessel first, but this would require an α–particle energy of ~0.3 MeV, less than the minimum detectable energy of the alpha collector. But if, for the sake of argument, one assumes that there are orbits that strike the bottom of the vessel first as they diffuse radially outwards, then the radial dependence of the anomalous loss can be used to calculate a diffusive step-size. Assuming that at every bounce the particles walk randomly with a step-size of b, and that they will be scraped-off by an obstacle (such as the RF limiters or the probe head) with a probability P_l, the α–particle flux at a distance x behind the obstacle is $I(x) = I_0(1 - P_l)^N$, where I_0 is the α–particle flux at x=0, and $N = (x/b)^2$ is the number of bounces needed for the particle to randomly walk the distance x [42]. The probability of scrape-off is estimated to be the ratio of the toroidal extent of the obstacles above x to the toroidal circumference of the vessel. It can easily be shown that the scrape-off on the probe head is insignificant compared to the scrape-off on the RF limiters. For the lower row of ports, with x=0.6 cm and $P_l \approx$0.13 (eight limiters that each have a toroidal extent above x of ~27 cm), the factor of 3 between rows results in a step-size of ~0.2 cm. Diffusion at this step-size down to the location of the scintillator detector, with x=1.2 cm and P_l ≈0.19 (toroidal extent of each limiter above x increased to ∼39 cm) occurs with a flux reduction by a factor of ∼2000 with respect to the upper row of ports, consistent with the absence of anomalous loss to the 90° scintillator detector.

A step-size of 0.2 cm per bounce corresponds to a diffusion coefficient, $D = b^2/\tau_b$, of ∼0.4 m^2/s, where τ_b ≈10μs is the bounce period. This results in a time scale for diffusion to the wall, $\tau_D \approx a^2/4D$, of ∼0.6 s. Assuming all the alphas diffuse at this rate, ∼30% of the α–particles should be lost to the wall within one energy e-folding time. However, small step-size diffusion to the bottom of the TFTR vessel probably isn't realistic since it is not consistent with high energy orbits that tend to scrape-off near the midplane. A larger step-size would result in a larger global loss, however, there would likely be a threshold condition such that not all of the α–particles are included in the diffusive process. Thus, without knowing the loss mechanism, it is difficult to estimate the global loss associated with the observed anomalous loss.

The large step-size of 17 cm inferred from the orbits of Fig. 4.17 is consistent with the 15 cm that was estimated in the same manner in Ref. [40] for delayed loss of 1.5 MeV (half the birth energy) DD fusion protons to the 90° scintillator detector for a R=2.45m, I_p=2.0 MA discharge. Thus the arguments as to the unlikeliness of pitch angle scattering, TF ripple, and MHD as possible causes of delayed loss [40] also apply to the 1.8 MA anomalous loss observed with the alpha collector probe, and will thus only be briefly summarized in the next section. Several new possibilities that attempt to explain the anomalous loss are also considered in the next section.

Possible explanations:	Anomalous loss features: a) absence on 90°scintillator	b) I_p dependence	c) total fluence	d) energy distribution	e) pitch distribution	f) radial distribution
1) Collisional Loss	X	?	X	O	X	?
2) TF ripple	?	?	X	X	O	?
3) MHD	?	?	X	?	?	?
4) CX Loss	X	O	O	O	O	X
5) I_p ramp down	X	O	O	X	?	?
6) Scattering	?	X	X	O	?	O
7) Activation	O	X	X	?	X	?
8) Foil surface fusion	X	X	X	O	?	O
9) Dif'n of residual He	O	X	?	X	?	O
10) Dif'n of implanted He	O	X	X	X	?	O

X - Inconsistent, O - Consistent, ? - Undecided

Table 4.2: *Anomalous Loss Explanations*

4.5 Possible Anomalous Loss Mechanisms

A model attempting to explain the mechanism responsible for the anomalous loss observed with the alpha collector would have to be consistent with the following features:

(a) Absence of anomalous loss on the 90° lost alpha scintillator detector in DT.

(b) I_p dependence - occurs at 1.8 MA but not at 1.0 MA.

(c) Total fluence - ≈6 times larger than first orbit loss.

(d) Energy distribution - peak ∼2.5±0.3 MeV inferred from shallow range distribution.

(e) Pitch angle distribution - peak ∼7±7° above the passing-trapped boundary, and most likely concentrated in narrow region above this boundary.

(f) Radial dependence - factor of 3 decrease from upper to lower row (separated by 1.1 cm).

The anomalous loss mechanisms described in the following sections are summarized in Table 4.2 with respect to their consistency with the observed loss features.

4.5.1 Collisional Loss

The $\sim$0.2 sec time delay observed on the 90° scintillator detector for delayed loss suggests a classical collisional loss mechanism, since this time is on the order of the slowing down time for fusion products [34]. Although large pitch angle scattering is capable of causing a confined orbit to become lost, it is too infrequent to be of significance, occurring on a time scale of >10 sec.

Small pitch angle scattering of barely passing α–particles into the first orbit loss cone can generate a diffusion of α–particles across the passing-trapped boundary, resulting in collisional nonprompt loss (Sec. 2.4.1). The α–particles that are subsequently lost should be marginally trapped, i.e. they should appear at the detector at the pitch angle of the passing-trapped boundary ($\sim$56° at 1.8 MA). However, delayed loss is seen to occur at pitch angles clearly above the passing-trapped boundary. This also appears to be the case with the alpha collector anomalous loss at 1.8 MA (Sec. 4.3.3). Furthermore, models consistently predict small loss fractions for collisional loss relative to first orbit loss. For instance, Ref. [34] reported a TRANSP prediction for an R=2.45 m, I_p=1.6 MA TFTR discharge of a global loss due to collisions of α–particles of 0.35%, which was only $\sim$5% of the calculated first orbit loss fraction for that shot.

4.5.2 Toroidal Field (TF) Ripple Effects

There are at least two different mechanisms through which TF ripple can cause radial transport of fast ions (Sec. 2.3.2). Stochastic ripple diffusion (SRD) [12] is a collisionless process which produces a radial step near the banana tip of those trapped particles that meet a particular threshold criterion. The maximum vertical step-size for 2.5 MeV α–particles in the conditions of discharge B can be shown to be $\approx$ 5 cm, in a manner similar to the calculation of Ref. [40] that estimated a $\approx$ 3.5 cm maximum step-size for 1.5 MeV protons in a 2 MA plasma. Therefore, even if a trapped particle passes through two banana tips before passing near the midplane, it can only gain up to a maximum of 10 cm outward displacement, significantly less than the 17 cm necessary to reach the alpha collector at the bottom of the vessel (Sec. 4.4.3). This relatively small step-size is such that almost all of the SRD loss should be localized within 30° of the outer midplane [10].

A synergistic enhancement of fast ion diffusion has been found for SRD with collisions [13]. This effect is simulated using the Hamiltonian guiding center drift orbit Monte Carlo code, gc-ORBIT [43] (not to be confused with the Lorentz ORBIT code). Under the conditions of the 1.0 MA discharges, this code predicts a global alpha loss of $\sim$25%. Only $\sim$15% of this global loss is 'delayed' (i.e. occurring below 3.5 MeV). For the conditions of the 1.8 MA discharges, this code predicts a global alpha loss of $\sim$4%, of which only $\sim$21% is 'delayed'. Thus, the synergistic enhancement is not of sufficient magnitude to make the 'delayed' losses at 1.8 MA much more significant than they are at 1.0 MA. Furthermore, these 'delayed' losses are clearly peaked poloidally within 30° below the outer midplane. It should be noted, however, that preliminary work involving improved modeling of the magnetic field in the vacuum gap region between the plasma and the first wall, by a group at the Kiev Institute for Nuclear Research, has indicated the possibility of half-energy alphas reaching the 90° detectors through this mechanism [44].

The other TF ripple effect that can cause radial transport of fast ions is super-banana trapping inside the ripple wells [40]. Particles lost through ripple well trapping would have pitch angles very close to 90°, causing most of them to be self-shadowed by the probe head, as shown in Fig. 4.13. Note that a true pitch angle of 90° corresponds to a toroidal pitch angle of $\sim$85° due to the $\sim$5° offset between true and toroidal pitch angles (Sec. 4.3.3). The detection of the partially thermalized anomalous loss in the foil stack in the 30° collimating port of exposure B (Fig. 4.6(b)) indicates that the anomalous loss extends down to toroidal pitch angles below 75° (Sec. 4.3.3). Furthermore, the left collection fraction analysis of Sec. 4.3.3 gives an estimate of 63°$\pm$7° for the toroidal pitch angle of the anomalous loss, slightly smaller than the $\sim$70° measured by the 90° scintillator detector for delayed loss. Ref. [40] concluded that it was unclear how particles lost through this mechanism could arrive at the detector with pitch angles this small. Most importantly, a loss of ripple well trapped particles at a true pitch angle of $\sim$90° would have a better likelihood of implanting into the foils in the 120° port than in the 75° port because the 75° port has a larger self-shadowing effect. However, the anomalous loss is not detected in the 120° foils. Thus, it seems unlikely that ripple well trapping could provide an explanation of the anomalous loss.

4.5.3 MHD Effects

The two mechanisms by which magnetic perturbations due to MHD activity can cause radial transport of high energy particles were considered with respect to delayed loss in Ref. [40]. These mechanisms are the parallel drift of the ion along radially perturbed field lines, and the perpendicular drifts across the field lines. Both the former mechanism and a non-resonant interaction of the latter, required an unrealistically large magnetic perturbation of $\tilde{B}_r/B_t \approx 10^{-2}$ to achieve a 10 cm step-size [40], where $\tilde{B}_r$ is the local radial magnetic perturbation. The magnitude of normal magnetic perturbations inside plasmas is generally $\tilde{B}_r/B_t \approx 10^{-4}$ [45, 46]. Similarly, orbits resonant with the perturbation required the largest MHD perturbations in TFTR [40]. Thus it was concluded that the effects of some hidden MHD activity during seemingly MHD quiescent plasmas cannot easily explain the large last step necessary to bring the escaping orbit to the 90° detector [40]. This conclusion applies equally well to the MHD quiescent discharges conducted for the alpha collector exposures as it did to discharges examined for delayed loss.

4.5.4 Loss of He^+ from Charge Exchange with Impurities or NBI Neutrals

Another possibility is that fully stripped α–particles charge exchange (CX) with partially stripped impurities producing singly ionized α–particles through:

$$He^{++} + A^{+q} \rightarrow He^{+} + A^{+q+1} \tag{4.3}$$

where A^{+q} are plasma impurity ions. The singly ionized α–particle then has twice the gyroradius it had before charge exchange, resulting in a doubling of its banana width.

The orbits of previously confined α–particles may suddenly transition to prompt loss trajectories that take some of the α–particles to the detector.

Olson [47] concluded that for a 0.1% low charge state impurity concentration of oxygen (i.e. $\sim 1 \times 10^{11}$ cm^{-3}) in TFTR, the average time for single electron capture for 2.0 MeV He^{++} is ≈5 ms. This is much less than the ∼200 ms alpha slowing down time and hence could cause a net diffusion to the walls and be a previously unrecognized mechanism for α–particle transport in TFTR.

With the addition of carbon tiles, the main impurity in TFTR is now carbon, not oxygen. At Z_{eff} ≈1.5 the impurity concentration for carbon is ≈5%, with roughly the same radial profile as the electron density. At electron temperatures ∼10 keV most of this carbon is fully stripped (C^{+6}) in the core. PPPL's MIST code solves for the density of ions in each charge state using atomic physics appropriate for these low-density high-temperature plasmas [48]. MIST predicts a H-like carbon (C^{+5}) concentration of $\sim 5 \times 10^{9}$ cm^{-3} (∼0.01% n_e) in the core, which increases by a factor of ∼30 at the cooler plasma edge. The lower charge states of carbon are present in the core at concentrations reduced by a factor of 1000 or more in relation to C^{+5}.

Charge exchange cross sections calculated for the $He^{++} + C^{+5}$ collision system using two different methods are shown in Fig. 4.18. The classical-trajectory Monte-Carlo (CTMC) [49] method may not be appropriate in the energy range being considered due to unphysical capture to deeply bound states that only exist classically, resulting in cross sections that may be unrealistically large by up to a factor of about 5 at ∼2.5 MeV. A coupled-Sturmian (CS) calculation was done at Pennsylvania State University [50, 51] to check on the magnitude of this uncertainty. Fig. 4.18 shows the CTMC results to be a factor of ∼ 3 times larger than the CS results for 2.5 ± 1.0 MeV, the energy range of interest for the anomalous loss. The calculations of this section are based on the CTMC results which were obtained first, although they are probably less reliable. While these calculations support charge exchange loss as being consistent with anomalous loss features b–e of Table 4.2 (as discussed in the remainder of this section), features a and f are not supported by this mechanism. Therefore it was not deemed necessary to repeat the calculations using the CS results.

The CTMC charge exchange cross section is seen in Fig. 4.18 to be $\approx 1.3 \times$

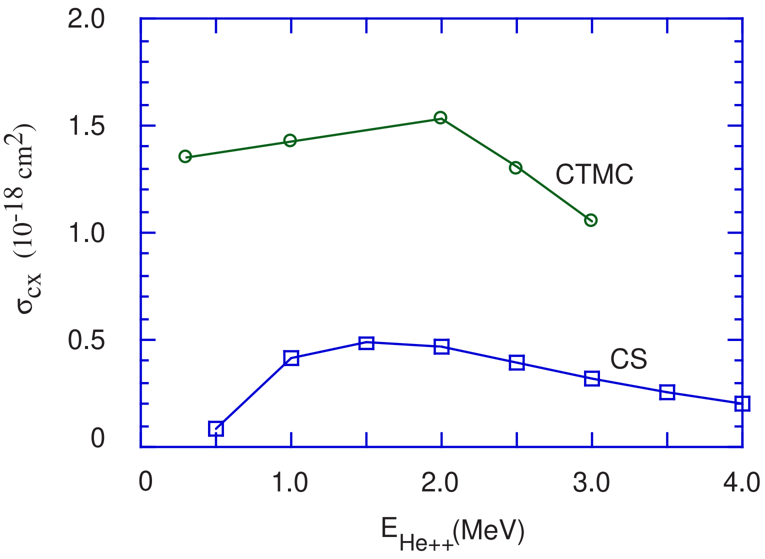

Figure 4.18: *Calculated single electron capture cross section for the He^{++} + C^{+5} collision system using the classical-trajectory Monte-Carlo method (CTMC) and the Coupled-Sturmian treatment (CS).*

10^{-18} cm^2 for alphas at 2.5 MeV. This results in a collision period for charge exchange of 2.5 MeV α–particles in the core of τ_{cx} ≈150 ms, which is of the same order as the alpha energy e-folding time, and a period of τ_{cx} ≈5 ms at the edge. Based on the CTMC calculations, therefore, charge exchange can be a significant factor in the evolution of α–particle orbits as they slow down.

Charge Exchange Orbits

Fig. 4.19 illustrates possible alpha orbit transitions due to charge exchange in a 1.8 MA plasma (exposure B) that can cause previously confined α–particles to strike the detector at the bottom of the vessel. Fig. 4.19(a) depicts a 2.5 MeV trapped α–particle that picks up an electron through charge exchange as it crosses the outer midplane on its counter-going leg and is subsequently lost to the detector. Fig. 4.19(b) depicts a 2.5 MeV counter-going passing α–particle that also charge exchanges as it crosses the outer midplane and is subsequently lost to the detector. A similar figure would show that co-going passing α–particles that charge exchange as they cross the

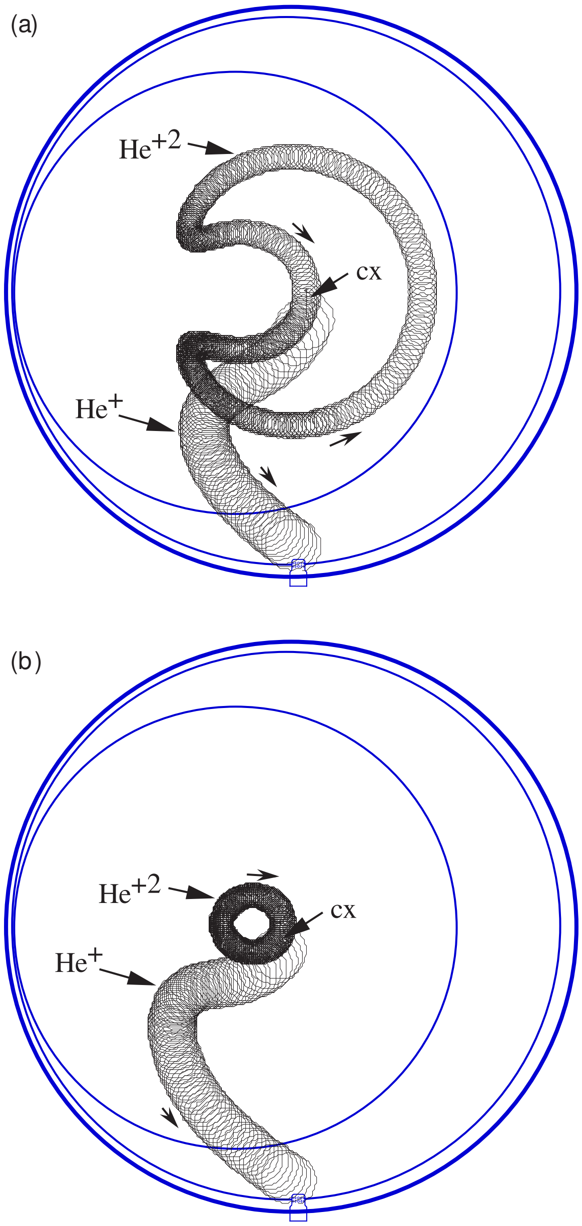

Figure 4.19: *2.5 MeV α–particle orbit transitions that take α–particles to the detector at 90° in R=2.45 m, I_p=1.8 MA plasmas for α–particles charge exchanging (cx) at (a) the outer-midplane crossing point of the counter-going leg of a trapped particle (R=270 cm, χ_t=63.5°), and (b) the outer-midplane crossing point of a counter-going passing particle (R=260 cm, χ_t=65.3°). Small arrows show direction of guiding center motion.*

inner midplane can also be subsequently lost to the detector on a co-going trajectory.

Fig. 4.20 illustrates what happens when α–particles charge exchange on the opposite side of orbits similar to those of Fig. 4.19. Fig. 4.20(a) shows that a 2.5 MeV trapped α–particle charge exchanging as it crosses the outer midplane on its co-going leg results in an orbit that passes closer to the magnetic axis. Similarly, Fig. 4.20(b) shows a 2.5 MeV counter-going passing α–particle that charge exchanges as it crosses the inner midplane also resulting in slight inward radial transport. Again, a similar figure would show that co-going passing α–particles that charge exchange as they cross the outer midplane also transport inwards. These particles are quickly reionized by the background plasma within a few poloidal transits, since the collision period for reionization in the core of $\sim 5\mu$s [31] is on the order of the bounce frequency of $\sim 10\mu$s. The lost orbits of Fig. 4.19, however, reach the detector within $\sim 3\mu$s, spending very little time in the core where the plasma density is peaked, and thus have a much lower probability of being reionized.

Figs. 4.19 and 4.20 represent the extremes in the orbit transitions possible through charge exchange. Charge exchange at other locations along an orbit results in less radial transport. A series of successive charge exchanges and reionizations could result in a large step-size radial diffusive process. However, as discussed in Sec. 4.4.3, the large radial step-size needed to bring the orbits to the detector is inconsistent with the factor of 3 reduction in fluence between the upper and lower rows of ports. It is not obvious how charge exchange loss could account for the radial dependence and absence of anomalous loss on the lost alpha scintillator detectors in DT. The larger downward drifts associated with the larger gyroradius of the He^+ should make shadowing by the nearby RF limiters less effective, and hence allow the charge exchange lost particles to easily reach the lower row of collimating ports on the alpha collector and the scintillator detector.

Plasma current dependence

Fig. 4.21 is a plot of toroidal pitch angle vs. r/a for the outer midplane crossing point

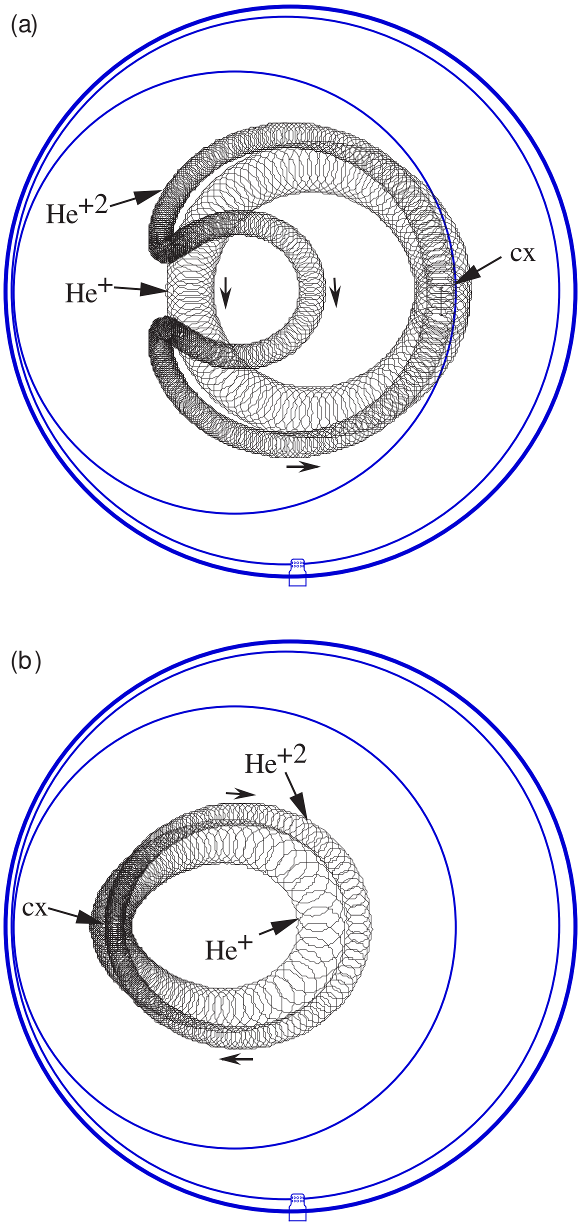

Figure 4.20: *2.5 MeV α–particle orbit transitions in R=2.45 m, I_p=1.8 MA plasmas for α–particles charge exchanging (cx) at (a) the outer-midplane crossing point of the co-going leg of a trapped particle (R=320 cm, χ_t=124°), and (b) the inner-midplane crossing point of a counter-going passing particle (R=200 cm, χ_t=70°), both resulting in inwards radial transport.*

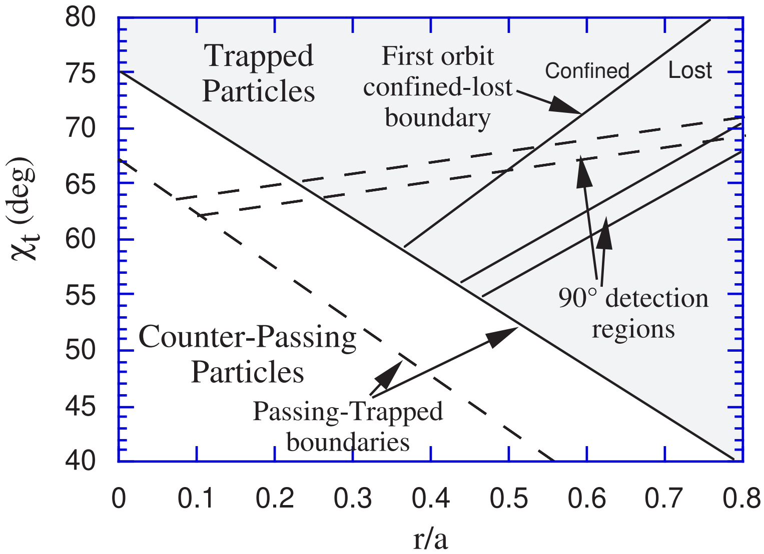

Figure 4.21: *Distribution of the different orbit classes for R=2.45 m, I_p=1.8 MA plasma in toroidal pitch angle versus their outer midplane crossing point for counter-going particles. Solid boundaries are for fully stripped 3.5 MeV α–particles. Dashed boundaries are for singly ionized 2.5 MeV α–particles representative of the anomalous loss.*

of counter-going particles in a 1.8 MA plasma. Both of these quantities are nearly conserved during an electron capture of the type shown in Fig. 4.19. The solid lines designate the boundaries for fully stripped 3.5 MeV α–particles. The passing/trapped boundary separates counter-passing orbits, which occur at low pitch angle or low minor radius, from trapped orbits (shaded region). The first orbit confined/lost boundary separates trapped confined orbits, which occur in the trapped region at high pitch angle or low minor radius, from trapped lost orbits. Within the region of trapped lost orbits is a subset of orbits, labeled as the 90° detection region, that intersect the detector at 90° below the midplane. The dashed lines designate the boundaries for singly ionized 2.5 MeV α–particles. All of the trapped 2.5 MeV singly ionized α–particles in this plot are lost in one poloidal orbit, thus there is no First Orbit Confined-Lost boundary for these particles. The region of 2.5 MeV singly ionized α–particles that intersect the vessel at 90° below the midplane are seen to correspond to previously first orbit confined (i.e. counter-passing and trapped confined orbits) 3.5 MeV fully stripped alphas all the way out to r/a $\approx$0.5, within which over 90% of the alphas are born for a standard alpha source distribution (i.e. parabolic to the eighth power). Therefore, nearly all of the 2.5 MeV singly ionized α–particle orbits that strike the 90° detector were previously confined.

An examination of α–particle orbits for a 1.0 MA plasma (producing a figure analogous to Fig. 4.21) has shown that all of the 2.5 MeV singly ionized α–particles that intersect the vessel at 90° below the midplane correspond to previously first orbit lost 3.5 MeV fully stripped α–particles. Therefore, there is no reservoir of confined α–particles at 1.0 MA available to take part in this loss mechanism, possibly explaining the absence of the anomalous loss at 1.0 MA.

Total fluence

The total fluence from this loss mechanism is estimated by modeling it as a new source of α–particles at a birth energy of 2.5 MeV, carrying a single charge, with an isotropic velocity distribution and the same radial source profile as the 3.5 MeV birth energy α–particles, allowing the use of the Lorentz ORBIT code. The predicted fluence of 2.5 MeV charge exchanged α–particles (i.e. He^{+}) to the 75° port of exposure B is a factor of 2 larger than the first orbit loss prediction under these assumptions. This falls short of the ratio of measured anomalous loss to predicted first orbit loss of 6 by a factor of 3. However, a flattening of the radial source profile from parabolic to the eighth to pure parabolic is sufficient to account for the full factor of 6. Flattening of the profile might be expected due to the peaking of the C^{+5} density profile on the edge of the plasma, making charge exchange more likely to occur there. Also, the assumption of an isotropic velocity distribution may affect the calculation.

A similar calculation (also assuming a new source of isotropic 2.5 MeV He^{+} with the same source profile as the 3.5 MeV He^{++}) using the gc-ORBIT code (Sec. 4.5.2) to predict the global first orbit loss (rather than to a particular detector) in exposure B, yields 22.2% global loss, a factor of ~8 larger than the 2.7% predicted for first orbit loss of 3.5 MeV α–particles. And the loss to a poloidally localized region of the wall about 90° where the detector is located is ~6 times larger for 2.5 MeV He^{+} than for 3.5 MeV He^{++}. The factor of 3 difference between the Lorentz ORBIT and gc-ORBIT predictions at 90° is probably due to the different projections that the singly and doubly charged alpha orbits that are collected by the detector would make on the wall. This implies that the 2.5 MeV He^{+} orbits collected by the detector would project onto an area of the wall ~3 times smaller than the 3.5 MeV He^{++}, owing to the fact that the larger downward drift of the 2.5 MeV He^{+} causes them to strike the wall at angles closer to normal incidence thus creating a smaller projection. While these are just rough estimates of charge exchange loss, they do indicate that this mechanism might be capable of generating losses on the order of magnitude of the observed anomalous loss.

To get a more realistic estimate of the total loss it will be necessary to develop or modify a guiding center following code to include charge exchange and reionization as a function of α–particle energy during the slowing down process. This code would also need to take into account the radial dependence of the charge exchange and reionization probabilities since charge exchange is more likely to occur at the edge where the C^{+5} density profile is peaked, and reionization is more likely to occur in the core where the plasma density profile is peaked.

Pitch angle distributions

The pitch angle distributions for first orbit loss of 3.5 MeV He^{++} and charge exchange loss of 2.5 MeV He^{+} calculated by the Lorentz ORBIT code as described above are shown in Fig. 4.22. The peak of the 2.5 MeV He^{+} distribution occurs $\sim 6°$ higher in toroidal pitch angle than it does for the first orbit loss of 3.5 MeV He^{++}. This is consistent with the inference that the anomalous loss peaks at a pitch angle $\sim 7° \pm 7°$ above the passing-trapped boundary for first orbit loss (Sec. 4.3.3). It is not clear that the shape of the pitch angle distribution for charge exchange loss would be the same as that calculated by treating it as a first orbit loss of 2.5 MeV He^{+}, but the peak is likely to remain fixed at 62° since this corresponds to the passing-trapped boundary for 2.5 MeV He^{+} in a 1.8 MA plasma.

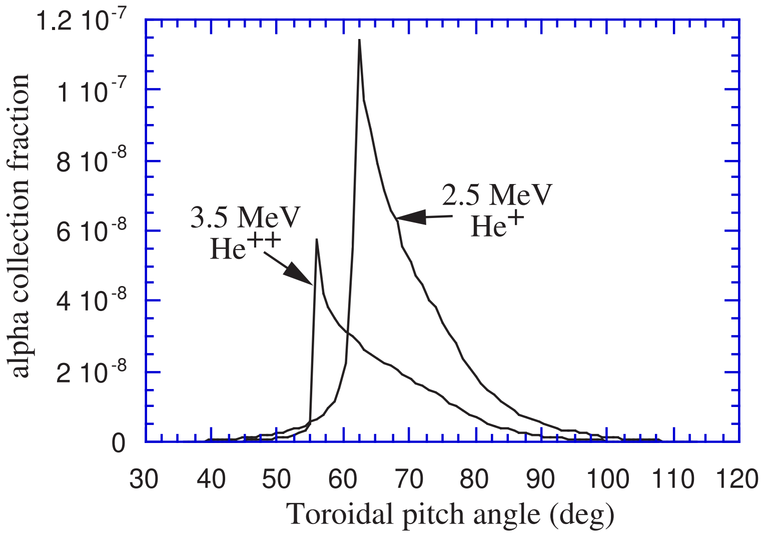

Figure 4.22: *Toroidal pitch angle distributions calculated at the detector for 3.5 MeV fully stripped α–particles and 2.5 MeV singly ionized α–particles in a R=2.45 m, I_p=1.8 MA plasma, assuming the same source profile and an isotropic velocity distribution in each case.*

Energy distribution

The energy distribution of charge exchange lost particles can be estimated by calculating the probability of charge exchange throughout the slowing down process. The probability for charge exchange at energy E, over a small period, Δt, such that E is fairly constant is:

$$P_{cx} = 1 - e^{-\Delta t/\tau_{cx}(E)} \tag{4.4}$$

where the collision period for charge exchange, τ_{cx}, is calculated as a function of energy as the α–particle slows down using Fig. 4.18. The time to slow down by 0.25 MeV increments is estimated from:

$$\frac{dE}{dt} = -\frac{E}{\tau_{sd}} \approx \frac{\Delta E}{\Delta t} \tag{4.5}$$

where τ_{sd} is the slowing down time (i.e. energy e-folding time) in the core. Reionization is neglected such that once an α–particle undergoes charge exchange it is assumed that it is no longer available to charge exchange at a lower energy. The resulting energy distribution is shown in Fig. 4.23 for three different slowing down

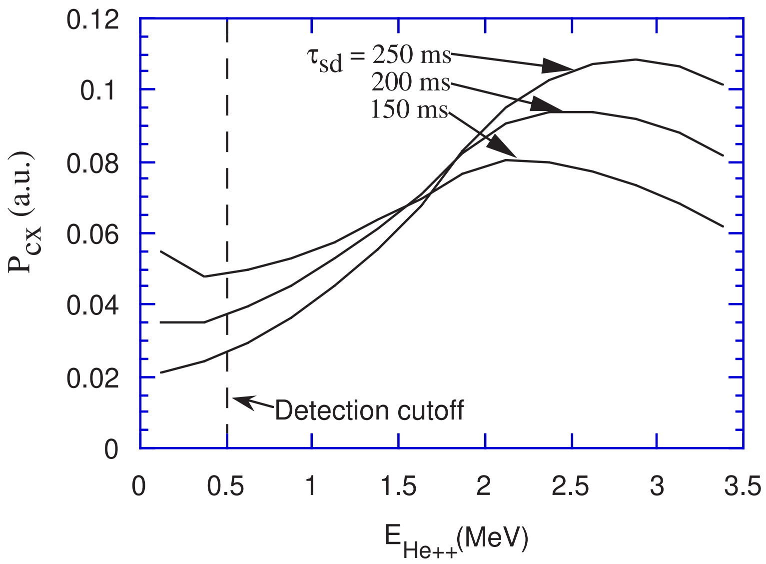

Figure 4.23: *Calculated probability of charge exchange versus α–particle energy. Assuming α–particles are lost only on their first charge exchange event, this plot represents the expected energy distribution of charge exchange lost α–particles.*

times. The inferred energy of the peak of the anomalous loss of 2.5$\pm$0.3 MeV is seen to be consistent with $\tau_{sd} = 200 \pm 50$ ms. The higher anomalous loss energy inferred from exposure D (2.7$\pm$0.3 MeV) as compared to exposure B (2.2$\pm$0.3 MeV) (see Sec. 4.3.2) might be explained by the longer slowing down time of the hotter plasma in exposure D (Table 4.1). At a slowing down time of 200 ms, $\sim$90% of α–particles are calculated to charge exchange before slowing down below the minimum detection energy of 0.5 MeV.

NBI neutrals

The other potential donors of electrons present in significant quantities are the NBI neutrals [52]. In this case, the velocity of the donor (i.e. the neutral beam species) must be taken into consideration since it is an appreciable fraction of the α–particle velocity. For instance, a 100 keV deuteron travels at about a third the speed of a 2.0 MeV α–particle. The cross section for charge exchange between a fully stripped 2.5 MeV α–particle and a neutral 100 keV deuteron reaches a maximum of $\sim 10^{-18}$ cm^2 when they are traveling in the same direction, and a minimum of $\sim 10^{-21}$ cm^2 when they are traveling in opposite directions [53]. Using the maximum of 10^{-18} cm^2 to obtain a conservative estimate, and assuming a density of NBI neutrals of $\sim 10^9$ cm^{-3} and a beam volume to plasma volume ratio of ~0.01 to account for the beam localization results in a collision period of ~70 sec. Thus, this process is insignificant in comparison to impurity charge exchange and slowing down.

The delayed loss observed by the scintillator detectors in DD might be caused by a similar mechanism. Since the DD fusion products are only singly ionized, charge exchange results in neutralization and subsequent straight line trajectories. Reionization in the plasma might allow some of these fusion products to transition to prompt loss orbits [52]. The differing mechanisms might account for the detection of the anomalous loss only in DD plasmas for the scintillator detectors.

The preceding calculations based on the CTMC cross sections show that CX loss may be consistent with many of the anomalous loss features. However, this loss mechanism is not consistent with the radial distribution of the anomalous loss nor its absence on the 90° scintillator detector.

4.5.5 Loss during I_p Rampdown

As the plasma current is ramped down at the end of a plasma discharge, remaining high energy α–particles become deconfined as the downward ∇B and curvature drifts become dominant. However, the I_p ramp down in exposure B doesn't start until 500 ms after the end of NBI and since the energy e-folding time (τ_{sd}) due to electron drag remains <200 ms, as shown in Fig. 4.24, in the plasma core during this time, the α–particle energy should have dropped by several factors of e by the start of the I_p ramp. Just two e-folding times are sufficient to reduce the α–particle energy below the detector's minimum detectable energy of 0.5 MeV. The observed peak in the energy distribution occurs at an energy only ~30% lower than 3.5 MeV and so, assuming there are no accelerating forces acting on the α–particles during the ramp down, cannot be attributed to anything that occurs >100 ms after the end of NBI.

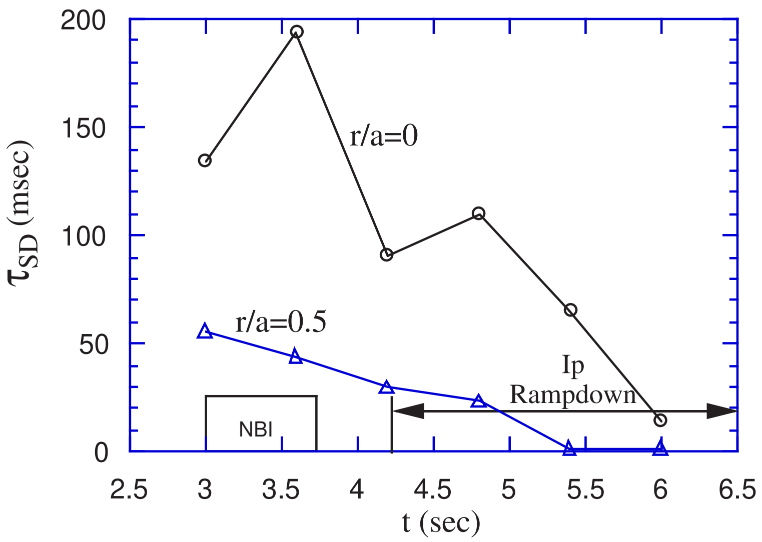

Figure 4.24: *Slowing down times calculated for r/a=0 and r/a=0.5 as a function of time in the discharge of exposure B.*

The induced toroidal electric field associated with the I_p ramp down can, however, cause a positive acceleration of counter-going passing α–particles. But this toroidal acceleration causes them to become more passing, which is not consistent with the detection of co-going particles. Furthermore, if there is a significant lower energy loss occurring after NBI, it should be visible to the lost alpha scintillator detectors, but it has never been observed. Therefore, a partially thermalized loss due to the current ramp down at the end of the discharge is not a viable explanation of the anomalous loss data.

It should be mentioned that the I_p ramp down in exposure D begins just 200 ms after the end of NBI, which was extended by 300 ms to increase the total alpha fluence to the collector probe. In Sec. 4.3.2 the peak in the alpha energy distribution was inferred to be $\sim$2.7$\pm$0.3 MeV for exposure D. This is $\sim$0.5 MeV higher than the peak of exposure B which had a 500 ms delay between the end of NBI and the beginning of the I_p ramp down. The higher anomalous loss energy associated with the shorter delay may be an indication that the anomalous loss mechanism does occur after the end of NBI, although, as mentioned above, this is highly unlikely. A scan of the delay time between NBI and the ramp start time could resolve this issue.

4.5.6 Scattering off RF Limiters and Collimator Walls

Scattering off of RF limiters and the wall of a collimating port can reduce the energy spectrum of the incoming α–particles. However, it is unlikely that scattering could explain the anomalously large alpha fluence observed in the 1.8 MA plasmas since this is not a new source of α–particles. It is also unlikely that there will be a significant contribution of scattered α–particles in the foil samples since large angle deflections of α–particles are quite rare in solids. TRIM-95 simulations (Sec. 4.2.2) of 3.5 MeV α–particles implanting into carbon at shallow angles result in just 20% of the implanted α–particles reemerging from the face of a flat piece of carbon when implanted at an angle of incidence of 89° (1° grazing angle), and less than 1% at 85°. In other words, most of the α–particles that enter a limiter or the wall of a collimating port will be stopped (within $\sim$11μm) without reemerging. Bench top implants using aluminum collimators with ^{241}Am alpha sources were done for calibration purposes. Results showed reasonable agreement to the predicted fluence and range distribution (Sec. 3.4.2). Furthermore, it is unlikely that the plasma current dependence could be explained by scattering.

4.5.7 Activation of Surrounding Materials

Activation of materials in first wall components by absorption of 14 MeV fusion neutrons and the subsequent release of α–particles through (n,α) reactions is very unlikely as a possible explanation of the anomalous loss. The largest cross sections for (n,α) reactions from 14 MeV neutrons are on the order of 10^{-25} cm^2 [54]. Using this conservatively large cross section (even though it is unrealistic for the materials in the first wall) results in a mean free path for a 14 MeV neutron of $\sim$100 cm in solid density. Assuming the resulting α–particles can escape from within 10μm of the surface, the neutron fluence of $\sim 10^{11}$ neutrons/cm^2 yields $\sim 10^6$ alphas/cm^2, or about six orders of magnitude smaller than the levels detected by the alpha collector. Therefore, (n,α) reactions can not provide the flux levels needed to explain the anomalous loss.

The fact that most of the (n,α) reactions have half lives >10 sec [54] could allow the collector probe to integrate the alpha collection over an extended duration even after the shot is over, possibly explaining the absence of the anomalous loss on the real time scintillator detectors. However, it would be difficult to explain the pitch angle distribution and plasma current dependence of the anomalous loss with such a mechanism.

4.5.8 Foil Surface Fusion

Another possibility that must be considered is that NBI D & T ions at 100 keV may be striking the surface of the foil and the walls of the collimating ports and fusing with D & T that are on the surface. This would give rise to an alpha source with a nearly isotropic velocity distribution near the surface of the foils. These α–particles wouldn't have to undergo any collimation so could implant at large incident angles ($0°$ being normal to the surface) explaining the shallow depth distribution. However, the deeper collimating ports of the redesigned probe head were intended to exclude NBI ions while allowing α–particles, which have $\sim 3\times$ larger gyroradius, to still implant (Sec. 4.3). It can be inferred from the fact that the anomalous loss features remained essentially unchanged between the two designs that foil surface fusion was not significant. This mechanism can also be ruled out on the basis of the current dependence. As I_p increases, the confinement of NBI ions should increase, providing less of a source of fusion on the foil surface.

4.5.9 Diffusion of Residual He

Residual He in the tokamak, leftover from previous experiments or from alpha ash, will not reach MeV energies during a discharge with no RF. The first Ni foil layer should stop α–particles below 0.5 MeV. If the foils are heated sufficiently to allow diffusion of this He into the deeper foil layers there should be a monotonic decrease in the alpha fluence with layer depth from a peak in the shallowest layer. Thus diffusion of residual He can not account for the peaks in the fourth and fifth layers of the 1.8 MA exposures.

Furthermore, it is unlikely that the current dependence of the anomalous loss could be explained by diffusion of residual He since the improved confinement associated with the higher plasma current should reduce heating of collector foils. Diffusion of residual He may, however, explain the low energy anomalous loss observed in 1.0 MA discharges.

4.5.10 Diffusion of Implanted He

The diffusion of implanted He from layer to layer between the time of implantation and removing the foils from the spool piece cannot explain the anomalously large fluence associated with the 1.8 MA data. Furthermore, if implanted He does diffuse, it should diffuse in both directions and not just toward the shallower layers as implied by the 1.8 MA data.

4.6 Summary, Conclusions, and Suggestions for Future Work

See Sec. 6.2 of the Conclusions Chapter for a summary, conclusions, and suggestions for future work.